

# Fast Compartment Model Calibration using Annealed and Transformed Variational Inference

Dongkyu Cho<sup>1</sup>, Won Chang<sup>3</sup>, and Jaewoo Park<sup>1,2</sup>

<sup>1</sup>Department of Statistics and Data Science, Yonsei University

<sup>2</sup>Department of Applied Statistics, Yonsei University

<sup>3</sup>Division of Statistics and Data Science, University of Cincinnati

November 23, 2022

## Abstract

Compartment models are widely used in climate science, epidemiology, and physics, among other disciplines. An important example of a compartment model is susceptible-infected-recovered (SIR) model, which can describe disease dynamics. Bayesian inference for SIR models is challenging because likelihood evaluation requires solving expensive ordinary differential equations. Although variational inference (VI) can be a fast alternative to the traditional Bayes approaches, VI has limited applicability due to boundary issues and local optima problems. To address these challenges, we propose flexible VI methods based on deep generative models that do not require parametric assumptions on the variational distribution. We embed a surjective transformation in our framework to avoid posterior truncation at the boundary. We provide theoretical conditions that guarantee the success of the algorithm. Furthermore, our temperature annealing scheme can avoid being trapped in local optima through a series of intermediate posteriors. We apply our method to variants of SIR models, illustrating that the proposed method can provide fast and accurate inference compared to its competitors.

*Keywords:* compartment models; variational inference; deep generative model; temperature

## 1 Introduction

Computer models have been widely used to simulate complex processes in many disciplines, including engineering, climate science, and epidemiology. Computer model calibration, a formal statistical procedure to find plausible sets of input parameters, is crucial to generate realistic projection (e.g. Kennedy and O'Hagan, 2001, Bayarri et al., 2007, Higdon et al., 2008, Tuo and Wu, 2015, Plumlee, 2017, 2019). One important example is susceptible-infected-recovered (SIR) compartment models (Kermack and McKendrick, 1927, Dietz, 1967), which describes the disease dynamics through ordinary differential equations (ODEs). Although Bayesian approaches have been developed, they can be computationally burdensome for complex SIR models because the algorithms require solving ODEs at each iteration. In this manuscript, we propose a fast variational inference (VI) approach for calibrating SIR models. By utilizing the deep generative methods, this new algorithm does not rely on a certain class of variational distribution, resulting in approximating highly complex posterior distribution. Furthermore, we adopt surjective transformation and temperature annealing to avoid inferential challenges in a naive VI approach.

Compared to the simulation-based Bayesian algorithms such as Markov chain Monte Carlo (MCMC) or approximate Bayesian computation (ABC) (Beaumont et al., 2002, Marin et al., 2012), VI approaches (Blei et al., 2017, Kucukelbir et al., 2017) can quickly approximate complex posteriors through optimization. However, even with such computational gains, VI is of limited applicability in the compartment model calibration framework for the following reasons. First, the traditional VI requires strong model assumptions on the variational distribution, such as the class of the conditionally conjugate exponential family model and mean field approximations. Second, it is often required to impose range constraints on the parameters in compartment models. Although bijective transformations that map from constrained to unconstrained parameter space have been widely used, such transformations may result in undesirable boundary effects at the edge of the parameter space (Kucukelbir et al., 2017). Lastly, VI approaches often suffer from poor local optima problems for compartment models (Blei et al., 2017, Zhang et al., 2018) due to highly irregular posterior densities of input parameters.

To address such challenges, we propose a practical VI algorithm for calibrating SIR compartment models. Our annealed and transformed VI (ATVI) combines key ideas from surjective transformations and temperature annealing. We adopt a surjective function (Nielsen et al., 2020) that maps unconstrained to constrained parameter space to avoid boundary effects caused by bijective transformations. In addition, we provide theoretical conditions that guarantee the success of surjective transformation and suggest a practical choice for such transformation. Furthermore, we naturally embed the sequence of intermediate posteriors to avoid local optima issues, motivated by previous temperature annealing works (Neal, 2001, Katahira et al., 2008, Mandt et al., 2016).

There is growing literature on the deep generative models in the deep learning community. Deep generative models have shown usefulness in many tasks as they are easily scalable and can represent high-dimensional correlated structures (see Bond-Taylor et al. (2021) for a review). We propose a practical tool for calibrating compartment models by combining the deep generative model and VI frameworks. To the best of our knowledge, this is the first attempt to study deep learning-based VI for calibrating compartment models. Through several challenging SIR compartment model examples, we observe that our method is faster than the traditional Bayes approaches (e.g., MCMC, ABC) while accurate compared to a naïve VI.

The outline for this paper is as follows. In Section 2, we introduce the background for SIR compartment model calibration. In Section 3, We discuss the application of deep learning-based VI to the compartment models and the inherent challenges. In Section 4, we propose ATVI by adapting surjective transformation and embedding temperature annealing schemes. In Section 5, we study the performance of ATVI through simulated and real infectious disease model examples. We conclude with a discussion in Section 6.

## 2 Background

### 2.1 Susceptible-Infected-Recovered Model (SIR)

Susceptible-infected-recovered (SIR) models (Kermack and McKendrick, 1927, Dietz, 1967) are a popular class of compartmental models for studying infectious disease dynamics. Hosts within

a population are categorized as susceptible ( $S$ ), infected ( $I$ ), and recovered/removed ( $R$ ), which are mutually exclusive groups. If hosts are exposed to diseases but are not infected yet, they are susceptible. They are infected if the pathogen has already spread to them. If their immune system successfully removes the pathogen, they are classified as recovered (or “removed” if they die). Let  $S, I, R$  denote the number of susceptible, infected, and recovered hosts within a population size  $N$  ( $S + I + R = N$ ). Then the basic (deterministic) SIR model has the following ODE:

$$\begin{aligned}\frac{\partial S}{\partial t} &= -\frac{\beta I}{N} S \\ \frac{\partial I}{\partial t} &= \frac{\beta I}{N} S - \gamma I \\ \frac{\partial R}{\partial t} &= \gamma I.\end{aligned}\tag{1}$$

The dynamics resemble the intuitive movement of the epidemic, as model parameters control the population transitions between each compartment. In (1),  $\beta$  and  $\gamma$  respectively represent the transmission and recovery rate of the disease.  $1/\gamma$  can be interpreted as the average infectious period. The force of infection  $\beta I$  describes the rate of susceptibles acquiring an infectious disease. There is extensive literature on variants of SIR models depending on epidemics (cf. Bjørnstad et al., 2002, Keeling and Rohani, 2011, Pitzer et al., 2012) and inference for such models is crucial to provide meaningful epidemiological insights and accurate future projections.

## 2.2 Bayesian Calibration

While the compartment models, such as the SIR model and its variants, provide a helpful way to model the dynamics of infectious disease, they are subject to various sources of uncertainties surrounding the model. One important source of uncertainty is the parametric uncertainty, stemming from the fact that the proper values of the parameters in the SIR model (such as  $\beta$  and  $\gamma$  in Equation (1)) are not known *a priori* and hence need to be estimated based on the data. The statistical procedure for estimating these parameters are referred to as model calibration, and there has been a suite of studies on this topic in the literature (e.g. Kennedy and O’Hagan, 2001, Bayarri et al., 2007, Higdon et al., 2008, Chang et al., 2016, Tuo and Wu, 2015, Plumlee, 2017, 2019, Bhatnagar et al., 2022) over the recent decades.

For the problem of SIR model calibration, our goal is to estimate the input parameter  $\boldsymbol{\theta} \in \Theta$

based on the observed data  $\mathbf{D} \in \mathbb{R}^p$ . For the basic SIR model in (1), the dimension of the input parameter,  $d$ , is 2, while we have more parameters in the complicated SIR models. The observed data are typically in the form of a single or multiple time series, and therefore  $p$  is determined as (the number of time series)  $\times$  (the length of time series). The general calibration framework (Kennedy and O'Hagan, 2001) can be written as follows:

$$\mathbf{D} = A(\boldsymbol{\theta}) + \boldsymbol{\delta}. \quad (2)$$

where  $A(\boldsymbol{\theta})$  is the discretized outcome of the SIR model with the same format as  $\mathbf{D}$  at the input parameter setting  $\boldsymbol{\theta}$  and  $\boldsymbol{\delta}$  is the data-model discrepancy. Unlike problems in other fields such as climate science (Bhat et al., 2012, Chang et al., 2014, 2016, Bhatnagar et al., 2022), we do not expect that the discrepancy has complicated dependence structures and hence i.i.d. discrepancy term is enough for our calibration problem.

Let  $p(\mathbf{D}|\boldsymbol{\theta})$  be the likelihood function based on the model in (2) and  $p_{\boldsymbol{\theta}}(\boldsymbol{\theta})$  be the prior density of  $\boldsymbol{\theta}$ . Then we can construct the posterior density  $p_{\boldsymbol{\theta}}(\boldsymbol{\theta}|\mathbf{D}) \propto p_{\boldsymbol{\theta}}(\boldsymbol{\theta})p(\mathbf{D}|\boldsymbol{\theta})$  for the Bayesian inference. MCMC is a standard way to infer  $\boldsymbol{\theta}$  in such a situation. However, inference based on MCMC can be ineffective if running the forward model  $A(\boldsymbol{\theta})$  is computationally expensive due to the complex ODE structure in compartment models. In such a situation, obtaining a well-mixed chain can take several hours or more, making the MCMC-based Bayesian method unattractive to practitioners who often need to provide projections in a timely manner.

### 3 Variational Inference Using Normalizing Flows

#### 3.1 Variational Inference with Parameter Constraints

VI (Blei et al., 2017, Kucukelbir et al., 2017) approximates the posterior distribution through optimization instead of computationally expensive sampling procedures such as MCMC. The main idea is to approximate the target posterior density  $p_{\boldsymbol{\theta}}(\boldsymbol{\theta}|\mathbf{D})$  using a variational density  $q_{\boldsymbol{\theta}}(\boldsymbol{\theta}; \boldsymbol{\phi})$  where  $\boldsymbol{\phi}$  is the variational parameter. With respect to  $\boldsymbol{\phi}$ , we minimize the reverse Kullback-Leibler (KL) divergence between the variational density and the posterior as follows:

$$\text{KL}(q_{\boldsymbol{\theta}}(\boldsymbol{\theta}; \boldsymbol{\phi}) || p_{\boldsymbol{\theta}}(\boldsymbol{\theta} | \mathbf{D})) = \mathbb{E}_{q_{\boldsymbol{\theta}}(\boldsymbol{\theta}; \boldsymbol{\phi})} [\log p(\mathbf{D} | \boldsymbol{\theta}) + \log p_{\boldsymbol{\theta}}(\boldsymbol{\theta}) - \log p(\mathbf{D}) - \log q_{\boldsymbol{\theta}}(\boldsymbol{\theta}; \boldsymbol{\phi})]. \quad (3)$$

By ignoring the normalizing constant  $p(\mathbf{D})$  that is not relevant to the target parameter  $\boldsymbol{\theta}$ , we can obtain the evidence lower bound (ELBO) as

$$\mathcal{L} = \mathbb{E}_{q_{\boldsymbol{\theta}}(\boldsymbol{\theta}; \boldsymbol{\phi})} [\log p(\mathbf{D} | \boldsymbol{\theta}) + \log p_{\boldsymbol{\theta}}(\boldsymbol{\theta}) - \log q_{\boldsymbol{\theta}}(\boldsymbol{\theta}; \boldsymbol{\phi})]. \quad (4)$$

Then we maximize ELBO in (4), which is equivalent to minimizing the KL divergence (3). However, the ELBO in (4) cannot be directly applicable to compartment model calibrations because of parameter constraints. In many compartment models, including SIR models, parameters are constrained within certain ranges due to scientific implications.

To address this, we introduce a bijective transformation  $\mathcal{T} : \boldsymbol{\Xi} \rightarrow \boldsymbol{\Theta}$ , where  $\boldsymbol{\Theta}$  and  $\boldsymbol{\Xi}$  are the constrained and unconstrained parameter space, respectively (Kucukelbir et al., 2017). We denote  $\theta_i$  as the  $i$ th element of  $\boldsymbol{\theta} = (\theta_1, \theta_2, \dots, \theta_d)$ , and  $a_i, b_i$  as the lower, upper bound of the  $\theta_i$  respectively. The constrained space can be represented as a Cartesian product of the compact spaces as  $\boldsymbol{\Theta} = \prod_{i=1}^d [a_i, b_i]$ . Then the inverse mapping is  $\mathcal{T}^{-1}(\boldsymbol{\theta}) = \boldsymbol{\xi}$ , where  $\boldsymbol{\xi} \in \boldsymbol{\Xi} = \prod_{i=1}^d (-\infty, \infty)$ . With such variable transformation, we can represent the variational density as

$$\log q_{\boldsymbol{\theta}}(\boldsymbol{\theta}; \boldsymbol{\phi}) = \log q_{\boldsymbol{\xi}}(\boldsymbol{\xi}; \boldsymbol{\phi}) + \log \left| \det \frac{\partial \mathcal{T}(\boldsymbol{\xi})}{\partial \boldsymbol{\xi}} \right|. \quad (5)$$

By plugging (5) into (4), we can represent our objective function (4) as

$$\begin{aligned} \mathcal{L} &= \mathbb{E}_{q_{\boldsymbol{\theta}}(\boldsymbol{\theta}; \boldsymbol{\phi})} [\log p(\mathbf{D} | \boldsymbol{\theta}) + \log p_{\boldsymbol{\theta}}(\boldsymbol{\theta}) - \log q_{\boldsymbol{\theta}}(\boldsymbol{\theta}; \boldsymbol{\phi})] \\ &= \mathbb{E}_{q_{\boldsymbol{\theta}}(\boldsymbol{\theta}; \boldsymbol{\phi})} \left[ \log p(\mathbf{D} | \boldsymbol{\theta}) + \log p_{\boldsymbol{\theta}}(\boldsymbol{\theta}) - \log q_{\boldsymbol{\xi}}(\boldsymbol{\xi}; \boldsymbol{\phi}) - \log \left| \det \frac{\partial \mathcal{T}(\boldsymbol{\xi})}{\partial \boldsymbol{\xi}} \right| \right]. \end{aligned} \quad (6)$$

Then we can maximize the objective function with respect to  $\boldsymbol{\phi}$ , while considering the parameter constraints in  $\boldsymbol{\theta}$ .

### 3.2 Deep Approximate Distribution with Normalizing Flow

To approximate the variational density  $q_{\boldsymbol{\theta}}(\boldsymbol{\theta}; \boldsymbol{\phi})$ , we utilize normalizing flows (NF) (Papamakarios et al., 2021, Kobyzhev et al., 2020) that can learn a non-linear and invertible mapping from a simple

latent distribution to a target distribution. If we have a well-trained NF model  $f$ , we can simply sample a random vector  $\mathbf{z}_0 \in \mathbb{R}^d$  from a latent distribution with the density  $p_{\mathbf{z}_0}(\mathbf{z}_0)$ ; especially, we use the standard normal density for  $\mathbf{z}_0$ . Then we can supply  $\mathbf{z}_0$  to the NF model to obtain  $\xi = f(\mathbf{z}_0; \phi)$ ; here  $\xi$  becomes identical to a sample from our approximate distribution with the density  $q_\xi(\xi; \phi)$ . From now, we refer to the variational density as the approximate density as well. With the variable transformation, the approximate density can be represented as

$$\log q_\xi(\xi; \phi) = \log(p_{\mathbf{z}_0}(\mathbf{z}_0)) + \log \left| \det \frac{\partial f(\mathbf{z}_0; \phi)}{\partial \mathbf{z}_0} \right|. \quad (7)$$

The NF model is defined with a stack of invertible and differentiable functions. Starting from the initial distribution for  $\mathbf{z}_0$ , the approximate distribution gradually evolves through a series of computationally efficient transformations. As a result, the model can represent a highly complex approximate distribution with relatively low computational cost while utilizing all the computational and inferential tools for modern deep learning. Compared to other traditional methods, such as mean-field approximation (Zhang et al., 2018), the NF model does not have to rely on specific parametric forms of variational distribution.

Furthermore, the NF model has some significant advantages when used for VI. The NF model exploits a reparameterization trick, which represents the gradient estimate as a series of deterministic mapping of a latent distribution. This leads to a lower variance for the resulting estimator than the other stochastic gradient estimators (Kingma and Welling, 2013, Zhang et al., 2018). Unlike other deep generative models, the NF model provides a way to explicitly calculate the density  $q_\theta(\theta; \phi)$ , which removes the need for approximating the  $\log q_\theta(\theta; \phi)$  in (4). Due to such advantages, NF models have been widely used for variational inference (Rezende and Mohamed, 2015, Kingma et al., 2016, Berg et al., 2018). However, to our knowledge, this study is the first attempt to utilize NF models for compartment model calibration.

In this manuscript, we use a stack of real-valued non-volume preserving transformation layers (Real NVP) (Dinh et al., 2016) to construct the NF model  $f$ . For brevity, consider a single Real NVP layer with an input  $\mathbf{x} \in \mathbb{R}^{d_x}$  and an output  $\mathbf{y} \in \mathbb{R}^{d_x}$ . The Real NVP layer first splits the input vector into two parts as  $\mathbf{x} = [\mathbf{x}_1, \mathbf{x}_2]$  where  $\mathbf{x}_1 \in \mathbb{R}^{d_1}$  and  $\mathbf{x}_2 \in \mathbb{R}^{d_2}$ . Then, the

corresponding output vector  $\mathbf{y}$  is given by

$$\mathbf{y}_1 = \mathbf{x}_1 \quad (8)$$

$$\mathbf{y}_2 = \mathbf{x}_2 \otimes \exp(\sigma_1(\mathbf{x}_1)) + \sigma_2(\mathbf{x}_1), \quad (9)$$

$$\mathbf{y} = \pi([\mathbf{y}_1, \mathbf{y}_2]) \quad (10)$$

where  $\otimes$  is an element-wise multiplication, and  $\sigma_1 : \mathbb{R}^{d_1} \rightarrow \mathbb{R}^{d_2}$  and  $\sigma_2 : \mathbb{R}^{d_1} \rightarrow \mathbb{R}^{d_2}$  can be any flexible transformation functions. In our implementation, we use the standard multilayer perceptron model with rectified linear unit activation functions for  $\sigma_1(\cdot)$  and  $\sigma_2(\cdot)$ . Here,  $\pi : \mathbb{R}^{d_x} \rightarrow \mathbb{R}^{d_x}$  is a permutation function that shuffles elements of the vector in a fixed way. The permutation function ensures some elements unchanged due to (8) in the current layer being changed through (9) in the next layer.

Following Dinh et al. (2016), we use an exponential function in (9) to make the Real NVP layer invertible; one may choose other functions as long as they have a positive range. Real NVP is particularly useful for normalizing flow because it allows us to construct a complex function while ensuring that the Jacobian term can be easily evaluated. The Jacobian term for a single Real NVP layer is

$$\frac{\partial \mathbf{y}}{\partial \mathbf{x}} = \begin{bmatrix} \mathbf{I}_{d_1} & \mathbf{0} \\ \frac{\partial \mathbf{y}_2}{\partial \mathbf{x}_1} & \text{diag}(\exp(\sigma_1(\mathbf{x}_1))) \end{bmatrix},$$

where  $\text{diag}(\cdot)$  denotes a diagonal matrix whose elements are given by the argument. Regardless of the choices of  $\sigma_1(\cdot)$  and  $\sigma_2(\cdot)$ , the determinant can be easily computed because the Jacobian is a lower triangular matrix. In our context, we can easily compute the determinant term in (7). By generalizing the above, we can construct a deep generative model with multiple Real NVP layers, resulting in a highly flexible function with low computational cost; therefore, it is widely used for state-of-the-art flow models (Kingma and Dhariwal, 2018).

### 3.3 Challenges in Variational Inference

Compared to the standard MCMC algorithms, VI approaches scale well to larger datasets or high-dimensional problems. Furthermore, with the well-trained NF model, we can construct

a complicated form of variational distribution without depending on restrictive parametric assumptions. However, the direct application of these methods to compartment calibration is challenging due to the following reasons.

The first issue is local optima. If the approximate density  $q_{\theta}(\theta; \phi)$  does not cover (i.e., mismatch) all of the high-density regions of the target  $p(\mathbf{D}|\theta)$  at the beginning of the training, the mismatched region may never be discovered during optimization. Similar issues are reported in the literature (Regli and Silva, 2018, Turner and Sahani, 2011). Although several alternatives, such as the trust region update (Arenz et al., 2020) or employing different divergences (Ranganath et al., 2016) have been proposed, they are computationally expensive and require some simplifying assumptions in the form of variational density. Another possible solution is to start optimization with a well-constructed  $q_{\theta}(\theta; \phi)$  which does not have too much mismatch with  $p(\mathbf{D}|\theta)$ . We provide more details with a practical solution in Section 4.3.

Furthermore, standard VI suffers from boundary effect problems due to parameter constraints in compartment models. For illustration, consider a parameter  $\theta \in \Theta = [0, 1]$  with a logistic function  $\mathcal{T}$  which maps  $\xi \in \Xi$  to  $\theta \in \Theta$  (i.e.,  $\theta = \mathcal{T}(\xi) = 1/(1 + e^{-\xi})$ ), which is a common choice. Then with a variable transformation, we have

$$\begin{aligned} q_{\theta}(\theta; \phi) &= q_{\xi}(\xi; \phi) \left| \det \frac{\partial \mathcal{T}(\xi)}{\partial \xi} \right| \\ &= q_{\xi}(\xi; \phi) [\mathcal{T}(\xi)(1 - \mathcal{T}(\xi))] \end{aligned} \quad (11)$$

The representation in (11) prevents  $q_{\theta}(\theta; \phi)$  from having positive values near the boundary of the  $\theta$  (i.e., 0 or 1), because  $[\mathcal{T}(\xi)(1 - \mathcal{T}(\xi))] \rightarrow 0$  as  $\xi \rightarrow \pm\infty$ . Other bijective transformations, such as hyperbolic tangent, can also have boundary effect issues. When the target density  $p_{\theta}(\theta|\mathbf{D})$  has a positive mass at the boundary of  $\Theta$ , the approximate density by  $q_{\theta}(\theta; \phi)$  will have a substantial mismatch with  $p_{\theta}(\theta|\mathbf{D})$  near the boundary areas.

## 4 Annealed and Transformed Variational Inference

In this section, we propose an annealed and transformed VI (ATVI) method for compartment models. An outline of ATVI is described in Figure 1. Figure 1 illustrates how the initial latent

variable  $\mathbf{z}_0$  is sequentially transformed into the target parameter  $\boldsymbol{\theta}$ . Here, we propose a new temperature annealing scheme for VI to construct intermediate target distributions, approximated with multiple real NVP layers. These block structures allow us to generate samples in the unconstrained parameter space from an initial latent vector  $\mathbf{z}_0$ . Instead of using bijective transformation  $\mathcal{T}$  that can have boundary effect issues, we introduce a *surjective* transformation  $\mathcal{B}$  to make connections between  $\Theta$  and  $\Xi$ .

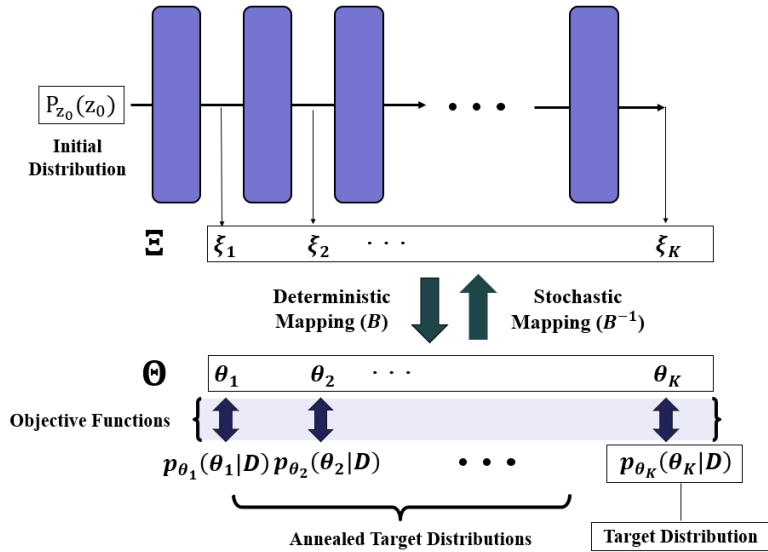


Figure 1: Illustration for the ATVI.

#### 4.1 Boundary Surjection

To address parameter constraint issues, we propose a new transformation, the boundary surjection. The boundary surjection guarantees the parameter constraints using a simple transformation. A mapping  $\mathcal{B} : \Xi \rightarrow \Theta$  is a deterministic and surjective mapping, which ensures that the mapping from  $\xi$  to  $\theta$  satisfies the parameter constraints. However,  $\mathcal{B}^{-1} : \Theta \rightarrow \Xi$  is not deterministic, and we refer to this inverse mapping as a stochastic transformation.

While most NF models are strictly bijective, Nielsen et al. (2020) suggested a stochastic and surjective transformation in their ‘SurVAE’ model. In this framework, the transformation is evaluated through a *likelihood contribution*, which works similarly to the Jacobian term in (5).

Nielsen et al. (2020) showed that for any distribution that is defined in  $\Xi$  or  $\Theta$ , a surjective transformation can be approximated as follows:

$$\mathbb{E}_{v_{\theta}(\theta|\xi)} [\log q_{\theta}(\theta; \phi)] \approx \log q_{\xi}(\xi; \phi) - \overbrace{\mathbb{E}_{v_{\theta}(\theta|\xi)} \left[ \log \frac{w_{\xi}(\xi|\theta)}{v_{\theta}(\theta|\xi)} \right]}^{\mathcal{V}(\theta, \xi)}, \quad (12)$$

where  $v$  and  $w$  are auxiliary probability densities. Here  $\mathcal{V}(\theta, \xi)$  is called the likelihood contribution. If the transformation is bijective, the likelihood contribution becomes deterministic and identical to the Jacobian term in (5). Nielsen et al. (2020) used their SurvAE model to impose the symmetry, permutation-invariance, or low dimensionality condition in learning the distribution of images or spatial fields. On the other hand, our surjective transformation focuses on alleviating boundary effect issues in calibration problems.

Consider the constrained parameter space  $\Theta = \prod_{i=1}^d [a_i, b_i]$ , which is defined through the Cartesian product of the compact spaces. Here, for each  $i$  we introduce a boundary surjection marginally through an augmented function  $g$  defined as follows:

$$g(\xi_i) = (\theta_i, s_i) = \begin{cases} (2b_i - \xi_i, 2), & \text{if } \xi_i > b_i, \\ (\xi_i, 1), & \text{if } a_i < \xi_i < b_i, \\ (2a_i - \xi_i, 0), & \text{if } \xi_i < a_i, \end{cases} \quad (13)$$

$$\xi_i = g^{-1}(\theta_i, s_i) = \begin{cases} 2b_i - \theta_i, & \text{if } s_i = 2, \\ \theta_i, & \text{if } s_i = 1, \\ 2a_i - \theta_i, & \text{if } s_i = 0. \end{cases} \quad (14)$$

Then the boundary surjection is given as  $\mathcal{B}(\xi_i) = g_1(\xi_i)$ , where  $g_1(\xi_i)$  and  $g_2(\xi_i)$  are the first and second component of the augmented function  $g(\xi_i)$ , respectively. Note that the transformation  $\mathcal{B}(\xi_i)$  is both surjective and non-injective  $\forall \xi_i \in \mathcal{B}^{-1}([a_i, b_i])$ . The constrained parameter value  $\theta_i$  is computed deterministically for a given value of  $\xi_i$ , but a tuple  $(\xi_i, s_i)$  cannot be obtained deterministically when  $\theta_i$  is given.

The auxiliary probability density  $v_{\theta_i}(\theta_i|\xi_i)$  in (12) can be decomposed as

$$v_{\theta_i}(\theta_i|\xi_i) = \sum_{s_i \in \{0,1,2\}} v_{\theta_i}(\theta_i|\xi_i, s_i) v_{s_i}(s_i|\xi_i). \quad (15)$$

Once we set the densities  $v_{\theta_i}(\theta_i|\xi_i, s_i)$ ,  $v_{s_i}(s_i|\xi_i)$  to be Dirac delta functions whose values are zero everywhere except at  $g_1(\xi_i), g_2(\xi_i)$  respectively, (15) becomes  $\sum_{s_i \in \{0,1,2\}} \delta(\theta_i - g_1(\xi_i)) \delta(s_i - g_2(\xi_i))$ . In a similar fashion, we can represent the other auxiliary probability density  $w_{\xi_i}(\xi_i|\theta_i)$  as

$$w_{\xi_i}(\xi_i|\theta_i) = \sum_{s_i \in \{0,1,2\}} w_{\xi_i}(\xi_i|\theta_i, s_i) w_{s_i}(s_i|\theta_i), \quad (16)$$

where  $w_{\xi_i}(\xi_i|\theta_i, s_i)$  to be a Dirac delta function whose values are zero everywhere except at  $g^{-1}(\theta_i, s_i)$  and  $w_{s_i}(s_i|\theta_i)$  is the conditional probability mass function for  $s_i$  given  $\theta_i$ . Then (16) becomes  $\sum_{s_i \in \{0,1,2\}} \delta(\xi_i - g^{-1}(\theta_i, s_i)) w_{s_i}(s_i|\theta_i)$ . Compared to (15), (16) is a stochastic transformation due to the randomness in  $s_i$ ; therefore, the inverse mapping  $\mathcal{B}^{-1}$  is stochastic. From (15) and (16), the likelihood contribution for each  $i$  can be simplified as

$$\begin{aligned} \mathcal{V}(\theta_i, \xi_i) &= \mathbb{E}_{v_{\theta_i}(\theta_i|\xi_i)} \left[ \log \frac{w_{\xi_i}(\xi_i|\theta_i)}{v_{\theta_i}(\theta_i|\xi_i)} \right] \\ &= \mathbb{E}_{\sum_{s_i} v_{\theta_i}(\theta_i|\xi_i, s_i) v_{s_i}(s_i|\xi_i)} \left[ \sum_{s_i} \log \frac{w_{\xi_i}(\xi_i|\theta_i, s_i) w_{s_i}(s_i|\theta_i)}{v_{\theta_i}(\theta_i|\xi_i, s_i) v_{s_i}(s_i|\xi_i)} \right] \\ &= \mathbb{E}_{\delta(\theta_i - g_1(\xi_i)) \delta(s_i - g_2(\xi_i))} \left[ \log \frac{\delta(\xi_i - g^{-1}(\theta_i, s_i)) w_{s_i}(s_i|\theta_i)}{\delta(\theta_i - g_1(\xi_i)) \delta(s_i - g_2(\xi_i))} \right] \\ &= \log w_{s_i}(s_i|\theta_i). \end{aligned} \quad (17)$$

In (17), the third line results from the fact that for an observed  $\xi_i$ ,  $v_{s_i}(s_i|\xi_i)$  takes a positive value only when  $s_i = g_2(\xi_i)$ . Similarly, the last equality holds because we defined  $g_1(\xi_i) = \theta_i$  and  $g_2(\xi_i) = s_i$  in (13). The joint likelihood contribution for all parameters can be written as  $\mathcal{V}(\boldsymbol{\theta}, \boldsymbol{\xi}) = \sum_{i=1}^d \mathcal{V}(\theta_i, \xi_i)$ . Similarly, we write the joint auxiliary densities as  $v_{\boldsymbol{\theta}}(\boldsymbol{\theta}|\boldsymbol{\xi}) = \prod_{i=1}^d v_{\theta_i}(\theta_i|\xi_i)$ , and  $w_{\boldsymbol{\xi}}(\boldsymbol{\xi}|\boldsymbol{\theta}) = \prod_{i=1}^d w_{\xi_i}(\xi_i|\theta_i)$ . Based on this simplified likelihood contribution, we summarize the transformed variational inference (TVI) algorithm in Algorithm 1.

In the following section, we will discuss modeling the conditional probability density  $w_{s_i}(s_i|\theta_i)$  and theoretical justifications of the TVI algorithm.

---

**Algorithm 1** Transformed Variational Inference (TVI) algorithm

---

1: Initialize  $\phi$ .

2: **while**  $\mathcal{L}$  not converged **do**

3:     Sample  $\{\mathbf{z}_0^{(j)}\}_{j=1}^m \sim p_{\mathbf{z}_0}(\mathbf{z}_0)$  and get  $\{\xi^{(j)}\}_{j=1}^m$  using  $\xi^{(j)} = f(\mathbf{z}_0^{(j)}; \phi)$

4:     Get  $\{\theta^{(j)}\}_{j=1}^m$  using  $\theta^{(j)} \leftarrow \mathcal{B}(\xi^{(j)})$

5:     Compute  $\mathcal{L}$ :

$$\mathcal{L} \leftarrow \frac{1}{m} \sum_{j=1}^{j=m} \left[ \log p(\mathbf{D}|\theta^{(j)}) + \log p_{\theta}(\theta^{(j)}) + \mathcal{V}(\theta^{(j)}, \xi^{(j)}) - \log q_{\xi}(\xi^{(j)}; \phi) \right]$$

6:     Update  $\phi$  by the gradient:  $\nabla_{\phi} \mathcal{L}$

7: **end while**

---

## 4.2 Theoretical Justification

For TVI algorithms, we provide theoretical justifications, including the necessary conditions of  $w_{s_i}(s_i|\theta_i)$ . We begin with the Proposition 1, which shows that a density function for  $\theta$  is exactly computed using the corresponding density function for  $\xi$  and the likelihood contribution  $\mathcal{V}(\theta, \xi)$ .

**Proposition 1.** *Consider  $p_{\theta}(\theta)$  and  $p_{\xi}(\xi)$  be some probability densities in the constrained and unconstrained space, respectively. If the support of the  $p_{\xi}(\xi)$  is a subset of  $\mathcal{B}^{-1}(\Theta)$ , then  $\log p_{\theta}(\theta) = \log p_{\xi}(\xi) - \mathcal{V}(\theta, \xi)$ .*

Proof of Proposition 1 is provided in the supplementary material. Proposition 1 indicates that there is no approximation error due to boundary surjection in the target space. Let  $p_{\theta}(\theta)$  and  $p_{\xi}(\xi)$  in Proposition 1 be  $p_{\theta}(\theta|\mathbf{D})$  and  $p_{\xi}(\xi|\mathbf{D})$ , respectively, then we have

$$\log p_{\theta}(\theta|\mathbf{D}) = \log p_{\xi}(\xi|\mathbf{D}) - \mathcal{V}(\theta, \xi).$$

For  $p_{\xi}(\xi|\mathbf{D})$ , the support condition is automatically satisfied. Similarly, if we set  $p_{\theta}(\theta), p_{\xi}(\xi)$  to be  $q_{\theta}(\theta; \phi), q_{\xi}(\xi; \phi)$  and the support of  $q_{\xi}(\xi; \phi)$  is a subset of  $\mathcal{B}^{-1}(\Theta)$ , we have

$$\log q_{\theta}(\theta; \phi) = \log q_{\xi}(\xi; \phi) - \mathcal{V}(\theta, \xi).$$

This implies that there is no approximation error for the approximate density.

However, caution is necessary to implement boundary surjection. First, we have to ensure that the support of  $q_{\xi}(\xi; \phi)$  is a subset of  $\mathcal{B}^{-1}(\Theta)$  during optimization. Second, the induced

target density  $p_{\xi}(\xi|\mathbf{D})$ , given by the boundary surjection, should not cause additional challenges in optimization. For example, a poorly curated boundary surjection may result in extra mode or discontinuity in  $p_{\xi}(\xi|\mathbf{D})$ , which makes it difficult to optimize  $\phi$  in  $q_{\xi}(\xi; \phi)$ .

To address these challenges,  $w_{s_i}(s_i|\theta_i)$  needs to be carefully curated. Our strategy is to introduce a boundary surjection radius,  $r$ . The main idea is to concentrate probability mass of  $p_{\xi}(\xi|\mathbf{D})$  inside  $\prod_{i=1}^d(a_i - r, b_i + r)$ , which ensure that the support of  $q_{\xi}(\xi; \phi)$  belongs to  $\mathcal{B}^{-1}(\Theta)$ . Moreover, we impose a set of conditions, including smoothness and continuity conditions to  $w_{s_i}(s_i|\theta_i)$ , which prevents having extra modes or discontinuities. For ease of exposition, we first consider the left side of the parameter boundary. We define  $w_{s_i}(s_i = 1|\theta_i) = u_i(\theta_i)$ , and  $w_{s_i}(s_i = 0|\theta_i) = 1 - u_i(\theta_i)$  where function  $u$  satisfies the following proposition.

**Proposition 2.** *Consider the following  $d$ -dimensional hypercubes:  $\mathcal{Q}_r(\mathbf{a}) = \prod_{i=1}^d[a_i - r, a_i + r]$ ,  $\mathcal{Q}_{r-}(\mathbf{a}) = \prod_{i=1}^d[a_i - r, a_i]$ , and  $\mathcal{Q}_{r+}(\mathbf{a}) = \prod_{i=1}^d[a_i, a_i + r]$ , which are obtained from the left side of the parameter boundary  $\mathbf{a} = (a_1, a_2, \dots, a_d)$  and for some radius  $r \in (0, \min_i\{\frac{b_i - a_i}{2}\})$ . Let  $p_{\theta}(\theta|\mathbf{D})$  be the target density such that  $0 < p_{\theta}(\theta|\mathbf{D}) \leq M < \infty$  and continuous for  $\theta \in \mathcal{Q}_{r+}(\mathbf{a})$ . Let  $q_{\xi}(\xi; \phi)$  be the approximate density that satisfies  $q_{\xi}(\xi; \phi) \in C^m(\mathcal{Q}_r(\mathbf{a}))$ ;  $C^m(\mathcal{S})$  is the class of  $m$  times differentiable functions over a set  $\mathcal{S}$ . If  $u_i$  satisfies the following conditions for some  $\epsilon > 0$  and  $\forall i$ :*

1.  $u_i \in C^{\infty}([a_i, \infty))$  such that  $u_i : [a_i, \infty) \rightarrow [0.5, 1)$  and monotone increasing.

2.  $u_i(a_i) = 0.5$ .

3.  $\forall R \in (r, \infty)$ ,  $u_i(a_i + R) \geq 1 - \sqrt[d]{\epsilon/M}$ .

4.  $\forall \mathbf{c} = (c_1, c_2, \dots, c_d) \in \mathcal{Q}_{r+}(\mathbf{a})$ ,  $\frac{\partial u_i(c_i)}{\partial c_i}(1 - u_i(c_i))^{-1} \geq \frac{\partial p_{\theta}(\mathbf{c}|\mathbf{D})}{\partial c_i}(p_{\theta}(\mathbf{c}|\mathbf{D}))^{-1}$ .

Then  $p_{\xi}(\xi|\mathbf{D}) \leq \epsilon$  for  $\xi \in \prod_{i=1}^d(-\infty, a_i - r) \cap \mathcal{B}^{-1}(\Theta)$ ,  $p_{\xi}(\xi|\mathbf{D})$  is continuous in  $\mathcal{Q}_r(\mathbf{a})$ , monotone increasing in  $\mathcal{Q}_{r-}(\mathbf{a})$ , and  $q_{\theta}(\theta; \phi) \in C^m(\mathcal{Q}_{r+}(\mathbf{a}))$ .

Proof of Proposition 2 is provided in the supplementary material. We now explain the implications of Proposition 2. First, by constructing the right side of the parameter boundary similarly, the proposition forces the transformed target distribution to be light-tailed, with most probability mass concentrated in  $\prod_{i=1}^d[a_i - r, b_i + r]$ . Note that  $\mathcal{B}^{-1}(\Theta)$  becomes  $\prod_{i=1}^d(\frac{3a_i - b_i}{2}, \frac{3b_i - a_i}{2})$

for finite  $a_i$  and  $b_i$ . If there is an one-sided parameter constraint (e.g.,  $\theta_i \in [a_i, \infty)$ ),  $\mathcal{B}^{-1}(\Theta) = (-\infty, \infty)$ . A light-tailed target distribution guides approximate distribution  $q_{\xi}(\xi; \phi)$  to concentrate its masses inside  $\prod_{i=1}^d (a_i - r, b_i + r)$ . This encourages the support of  $q_{\xi}(\xi; \phi)$  to be contained within  $\mathcal{B}^{-1}(\Theta)$  during model training, ensuring that the conditions for  $q_{\xi}(\xi; \phi)$  in Proposition 1 is satisfied. Second, the boundary surjection does not cause additional difficulties in approximating  $p_{\xi}(\xi | \mathcal{D})$ . The conditions in Proposition 2 ensures that  $p_{\xi}(\xi | \mathcal{D})$  is continuous, monotone increasing in  $(a_i - r, a_i)$ , and monotone decreasing in  $(b_i, b_i + r)$ ; therefore it does not introduce any extra modes. Inside the boundary, i.e., within  $\prod_{i=1}^d (a_i + r, b_i - r)$ , the transformed target  $p_{\xi}(\xi | \mathcal{D})$  is identical to the original target  $p_{\theta}(\theta | \mathcal{D})$ , and thus there is no additional distortion due to the transformation within that range. Intuitively, the transformed target distribution in  $\Xi$  is a “smoothly unfolded distribution” of the target distribution in  $\Theta$  near the parameter boundary. Lastly, the boundary surjection does not limit the smoothness of the  $q_{\theta}(\theta; \phi)$  with Proposition 2. This condition ensures that  $q_{\theta}(\theta; \phi)$  well approximates a target distribution, which typically has a smooth density function.

As we pointed out, the success of boundary surjection depends on the choice of the function  $u_i$  that should satisfy the conditions in Proposition 2. In what follows, we introduce a family of functions helpful in constructing  $u_i$ .

**Remark 1.** Consider the location-scale family of the logistic function,  $\varsigma_i(x; A, B) = \frac{1}{1+e^{-B(x-A)}}$ .  $\forall r \in (0, \frac{b_i - a_i}{2})$ , we can find  $A$  and  $B$  such that  $\varsigma_i(x; A, B)$  satisfies the first three conditions of Proposition 2. Also, the Condition 4 in Proposition 2 becomes

$$B\varsigma_i(c_i; a_i, B) \geq \frac{\partial p_{\theta}(\mathbf{c} | \mathcal{D})}{\partial c_i} (p_{\theta}(\mathbf{c} | \mathcal{D}))^{-1}. \quad (18)$$

Proof of Remark 1 is provided in the supplementary material. The Remark 1 demonstrates that a family of logistic functions can be used as the function  $u$ . We further note that as boundary surjection radius  $r$  gets smaller, the left hand side in (18) gets bigger, while  $\sup_{\mathbf{c} \in \mathcal{Q}_{r+}} \{ \frac{\partial p_{\theta}(\mathbf{c} | \mathcal{D})}{\partial c_i} (p_{\theta}(\mathbf{c} | \mathcal{D}))^{-1} \}$  gets smaller. Therefore, Condition 4 in Proposition 2 holds for a sufficiently small  $r$ .

We now revisit the example discussed in Section 3.3. As in (11), consider a parameter  $\theta \in [0, 1]$

with a boundary surjection function  $\mathcal{B}$ . The approximate density is now

$$q_\theta(\theta; \phi) = q_\xi(\xi; \phi) \exp(-\mathcal{V}(\theta, \xi)). \quad (19)$$

Compared to (11),  $\exp(-\mathcal{V}(\xi, \theta))$  has a positive value at the parameter boundary of  $\theta$ . Hence,  $q_\theta(\theta; \phi)$  does not distort the estimated density, and hence the constructed mapping does not have the boundary effect issue.

### 4.3 Sequentially Annealed Posteriors

Here, we propose a new temperature annealing scheme that modifies the standard NF framework by assigning a fixed sequence of annealed intermediate posterior distributions. We sequentially train each part of the model with the corresponding intermediate posterior in turn for a given pre-specified temperature schedule. To our knowledge, temperature annealing has not been utilized for variational inference with normalizing flows.

Sequentially annealed posteriors (SAP) first sets the sequence of temperature  $t^{(1)} > t^{(2)}, \dots, > t^{(K-1)} > t^{(K)} \equiv 1$ . Then the target posterior density  $p_\theta(\theta | \mathbf{D})$  with the  $k$ th temperature is

$$\log p_{\theta^{(k)}}(\theta^{(k)} | \mathbf{D}) = (1/t^{(k)}) \log p(\mathbf{D} | \theta^{(k)}) + \log p_\theta(\theta^{(k)}) + (1 - 1/t^{(k)}) \log p_{\mathbf{z}_0}(\theta^{(k)}) + C(t^{(k)}), \quad (20)$$

where  $C(t^{(k)})$  is a normalizing constant. Here  $p_{\mathbf{z}_0}(\cdot)$  is the density function of latent variable  $\mathbf{z}_0$  in the context of NF models; SAP evaluates the latent density at  $\theta$  and hence  $p_{\mathbf{z}_0}(\theta)$  is included in (20). The sequence of target distributions resembles that of annealed importance sampling (AIS) (Neal, 2001). The higher the temperature, the smaller the influence of the data information (likelihood) becomes, and hence the  $p_{\mathbf{z}_0}(\theta)$  (latent distribution) dominates. When the temperature reaches 1, the target distribution becomes the true posterior distribution with the density  $p_\theta(\theta | \mathbf{D})$ . The sequence of annealed target distributions is a natural extension of the NF model, which constructs a gradual change from  $p_{\mathbf{z}_0}(\theta)$  to  $p_\theta(\theta | \mathbf{D})$  (see Figure 1).

For each  $t^{(k)}$ , we introduce a block layer  $f^{(k)}(\cdot; \phi^{(k)})$  which is a composite of multiple NF layers. Here,  $\phi^{(k)}$  is the variational parameter in the NFs belonging to the  $k$ th block. Using a sequential composite up to the  $k$ th block layer, we generate  $\xi^{(k)}$  from the latent distribution as

$$\xi^{(k)} = (f^{(k)} \circ \dots \circ f^{(2)} \circ f^{(1)})(\mathbf{z}_0; \boldsymbol{\phi}^{(k)}, \dots, \boldsymbol{\phi}^{(2)}, \boldsymbol{\phi}^{(1)}), \quad \mathbf{z}_0 \sim N(\mathbf{0}_d, \mathbf{I}_d). \quad (21)$$

We let  $q_{\xi^{(k)}}(\xi^{(k)}; \boldsymbol{\phi}^{(k)}, \dots, \boldsymbol{\phi}^{(1)})$  be the  $k$ th variational density of  $\xi^{(k)}$ . By using the surjective function in (13), we can transform  $\boldsymbol{\theta}^{(k)} = \mathcal{B}(\xi^{(k)})$ . Then the variational objective for the  $k$ th block is given as follows:

$$\begin{aligned} \mathcal{L}^{(k)} = \mathbb{E}_{q_{\boldsymbol{\theta}^{(k)}}(\boldsymbol{\theta}^{(k)}; \boldsymbol{\phi}^{(k)}, \dots, \boldsymbol{\phi}^{(1)})} & [(1/t^{(k)}) \log p(\mathbf{D}|\boldsymbol{\theta}^{(k)}) + \log p_{\boldsymbol{\theta}}(\boldsymbol{\theta}^{(k)}) + (1 - 1/t^{(k)}) \log p_{\mathbf{z}_0}(\boldsymbol{\theta}^{(k)}) \\ & - \log q_{\boldsymbol{\theta}^{(k)}}(\boldsymbol{\theta}^{(k)}; \boldsymbol{\phi}^{(k)}, \dots, \boldsymbol{\phi}^{(2)}, \boldsymbol{\phi}^{(1)}) + C(t^{(k)})]. \end{aligned} \quad (22)$$

Here we train each block sequentially and separately from the first to the last in order. For the  $k$ th block, we optimize  $\boldsymbol{\phi}^{(k)}$  from (22), while fixing  $\boldsymbol{\phi}^{(1)}, \dots, \boldsymbol{\phi}^{(k-1)}$  obtained from the previous blocks. This allows us to drop the normalizing constant  $C(t^{(k)})$  in (20) because the temperature  $t^{(k)}$  is fixed within each block. This provides a substantial computational advantage compared to the adaptive temperature annealing methods (e.g. Mandt et al., 2016).

We initialize the parameters  $\{\boldsymbol{\phi}^{(k)}\}$  to be zero, which makes the neural networks  $\sigma_1$  and  $\sigma_2$  in (9) as zero functions; thus,  $f^{(k)}(\cdot; \boldsymbol{\phi}^{(k)})$  becomes an identity function. As a result, training of the  $k$ th block can start from a well-trained function  $f^{(k-1)} \circ \dots \circ f^{(2)} \circ f^{(1)}$ . By setting  $t^{(k)}$  to be lower than  $t^{(k-1)}$ , the intermediate approximate density  $q_{\boldsymbol{\theta}^{(k)}}(\boldsymbol{\theta}^{(k)}; \boldsymbol{\phi}^{(k)}, \dots, \boldsymbol{\phi}^{(2)}, \boldsymbol{\phi}^{(1)})$  reflects more information from the likelihood function  $p(\mathbf{D}|\boldsymbol{\theta}^{(k)})$ .

We now explain the benefit of our annealing algorithm from the perspective of minimizing the reverse KL divergence in (3). Without such annealing schemes, optimization based on reverse KL divergence can lead to local optima problems. This can especially happen when the approximate distribution covers only a part of the high-density region of the target distribution. Our approach alleviates this issue through a gradual learning strategy. When training the  $k$ th block, we initialize the  $k$ th block as  $q_{\boldsymbol{\theta}^{(k)}}(\boldsymbol{\theta}^{(k)}; \boldsymbol{\phi}^{(k)}, \boldsymbol{\phi}^{(k-1)}, \dots, \boldsymbol{\phi}^{(1)}) = q_{\boldsymbol{\theta}^{(k-1)}}(\boldsymbol{\theta}^{(k)}; \boldsymbol{\phi}^{(k-1)}, \dots, \boldsymbol{\phi}^{(1)})$  because  $f^{(k)}(\cdot; \boldsymbol{\phi}^{(k)})$  is initialized as an identity function. This reduces the distance between the approximate density  $q_{\boldsymbol{\theta}^{(k)}}(\boldsymbol{\theta}^{(k)}; \boldsymbol{\phi}^{(k)}, \boldsymbol{\phi}^{(k-1)}, \dots, \boldsymbol{\phi}^{(1)})$  and target density  $p_{\boldsymbol{\theta}^{(k)}}(\boldsymbol{\theta}^{(k)}|\mathbf{D})$  at the beginning of training of the  $k$ th block. Compared to the standard NF model that initializes the approximate density  $q_{\boldsymbol{\theta}}(\boldsymbol{\theta}; \boldsymbol{\phi})$  as  $p_{\mathbf{z}_0}(\boldsymbol{\theta})$ , our SAP approach is more effective in that it initializes

from the approximate density resembling  $p_{\theta^{(k-1)}}(\theta^{(k-1)}|\mathbf{D})$  that is much closer to  $p_{\theta^{(k)}}(\theta^{(k)}|\mathbf{D})$ .

#### 4.3.1 Last Temperature Fine Tuning

Reverse KL divergence and forward KL divergence have trade-off effects on variational inference tasks. Reverse KL divergence-based optimization is effective in capturing the mode of the target, while forward KL divergence-based algorithm can better capture the tail part of the target (Regli and Silva, 2018). Therefore, SAP may be further fine-tuned using forward KL divergence. Here, we use the reverse KL up to  $t^{(K-1)}$  temperature and apply the forward KL for the last temperature  $t^{(K)}$  to improve the tail part approximation.

However, forward KL divergence cannot be implemented in a naïve manner as it requires samples from the true target density. Forward KL divergence is implemented with importance sampling approximations to address this (Li and Turner, 2016, Bornschein and Bengio, 2014, Jerfel et al., 2021). The general framework can be written as follows:

$$\text{KL}(p_{\theta}(\theta|\mathbf{D})|q_{\theta}(\theta;\phi)) = \mathbb{E}_{q_{\theta}(\theta;\phi)} \left[ \frac{p_{\theta}(\theta|\mathbf{D})}{q_{\theta}(\theta;\phi)} (\log p_{\theta}(\theta|\mathbf{D}) - \log q_{\theta}(\theta;\phi)) \right] \quad (23)$$

Then we define the forward KL divergence variational objective as

$$\mathcal{L}_{fwd} = \mathbb{E}_{q_{\theta}(\theta;\phi)} [w(\log p(\mathbf{D}|\theta) + \log p_{\theta}(\theta) - \log q_{\theta}(\theta;\phi))], \quad (24)$$

where  $w \propto \frac{p(\mathbf{D}|\theta)p_{\theta}(\theta)}{q_{\theta}(\theta;\phi)}$  is the importance weight. Using Monte Carlo samples generated from the importance function  $q_{\theta}(\theta;\phi)$ , we can provide the importance sampling estimate of (24). However, this method is still not applicable when  $q_{\theta}(\theta;\phi)$  is far away from  $p_{\theta}(\theta|\mathbf{D})$ ; the variance of  $w$  goes to infinity. To stabilize these weights we use Pareto smoothed importance sampling (PSIS) for weight normalization (Vehtari et al., 2015). This method calculates truncated normalized importance weight  $\tilde{w}$  which is asymptotically unbiased and consistent with finite weight variance. However, the use of this approach greatly increases the computational cost because the importance sampling size has to be very large to ensure unbiasedness.

To circumvent this issue, we apply forward KL with PSIS only for the last temperature  $t^{(K)}$ . This strategy can reduce computational costs as well as can stabilize importance sampling weights. The well-trained approximate density  $q_{\theta^{(K-1)}}(\theta^{(K-1)}; \phi^{(K-1)}, \dots, \phi^{(1)})$  from the

$(K - 1)$ th block is close to  $p_{\theta^{(K-1)}}(\theta^{(K-1)} | \mathbf{D})$ , which is in turn similar to  $p_{\theta^{(K)}}(\theta^{(K)} | \mathbf{D})$ . By incorporating SAP in our context, we propose the annealed and transformed variational inference (ATVI) algorithm, which is summarized in Algorithm 2.

---

**Algorithm 2** Annealed and transformed variational inference (ATVI) algorithm

---

```

1: Initialize  $\phi$  and set the temperature ladder  $\{t^{(k)}\}_{k=1}^K$ .
2: for  $k = 1$  to  $K$  do
3:   while  $\mathcal{L}^{(k)}$  not converged do
4:     Sample  $\{\mathbf{z}_0^{(j)}\}_{j=1}^m \sim p_{\mathbf{z}_0}(\mathbf{z}_0)$  and get  $\{\xi^{(k),(j)}\}_{j=1}^m$  using (21)
5:     Get  $\{\theta^{(k),(j)}\}_{j=1}^m$  using  $\theta^{(k),(j)} \leftarrow \mathcal{B}(\xi^{(k),(j)})$ 
6:     Calculate  $\mathcal{L}^{(k)}$ :

$$\mathcal{L}^{(k)} \leftarrow \frac{1}{m} \sum_{j=1}^m \left[ \frac{1}{t^{(k)}} \log p(\mathbf{D} | \theta^{(k),(j)}) + \log p_{\theta}(\theta^{(k),(j)}) \right. \\ \left. + (1 - \frac{1}{t^{(k)}}) \log p_{\mathbf{z}_0}(\theta^{(k),(j)}) + \mathcal{V}(\theta^{(k),(j)}, \xi^{(k),(j)}) - \log q_{\xi}(\xi^{(k),(j)}; \phi) \right]$$

7:   If  $k = K$  do: (last temperature fine-tuning)
8:     Calculate truncated importance weight  $\tilde{w}^{(j)}$  using PSIS
9:     Calculate  $\mathcal{L}^{(k)}$ :

$$\mathcal{L}^{(k)} \leftarrow \frac{1}{m} \sum_{j=1}^m \tilde{w}^{(j)} \left[ \frac{1}{t^{(k)}} \log p(\mathbf{D} | \theta^{(k),(j)}) + \log p_{\theta}(\theta^{(k),(j)}) \right. \\ \left. + (1 - \frac{1}{t^{(k)}}) \log p_{\mathbf{z}_0}(\theta^{(k),(j)}) + \mathcal{V}(\theta^{(k),(j)}, \xi^{(k),(j)}) - \log q_{\xi}(\xi^{(k),(j)}; \phi) \right]$$

10:    Update  $\phi^{(k)}$  by the gradient:  $\nabla_{\phi^{(k)}} \mathcal{L}^{(k)}$ 
11:   end while
12: end for

```

---

## 5 Applications

In this section, we apply our approach to simulated and real compartment model examples. To illustrate the performance of our method, we compare ATVI with baseline Bayes approaches (e.g., ABC or MCMC) and a basic VI (without annealing and boundary surjection). We implement all algorithms in PyTorch. Except for an MCMC algorithm in Section 4.3, the computation times are based on AMD Ryzen 5 5600X 6-Core Processor 3.70 GHz and NVIDIA GeForce RTX 3090. For the MCMC algorithm, the code is implemented on AMD Ryzen 9 3900X 12-Core Processor 3.79 GHz to accelerate computation. The source code can be downloaded from

<https://github.com/CrawlingKiming/AdVI>.

### 5.1 SIR Model Example

Here, we simulated an epidemic from a basic SIR model (1). For given initial conditions  $S_0 = 99$ ,  $I_0 = 1$ ,  $R_0 = 0$  and true parameters  $\beta = 1.5$ ,  $\gamma = 0.5$ , simulations were run for 17 days. We assume that the infected and recovered population can only be observed with Gaussian error  $\epsilon \sim \mathcal{N}(0, 0.1)$ . We used uniform priors of model parameters over a plausible range as in Minter and Retkute (2019). We provide details about priors in the supplementary material.

For VI and ATVI, we use 20 layers of flow model with 125 gradient updates. We set the learning rate as  $8 \times 10^{-4}$  for both approaches, which can guarantee convergence in our example. For ATVI, we set the temperature ladder as  $(t^{(1)}, t^{(2)}) = (100, 1)$ ; each block contains ten layers of the flow model. As the baseline competitor, we also implement the ABC-rejection algorithm by following the same settings in Minter and Retkute (2019).

	ATVI	VI	ABC
$\beta$	1.49 (0.030)	1.49 (0.075)	1.51 (0.039)
Coverage (%)	100	98	100
$\gamma$	0.50 (0.009)	0.50 (0.011)	0.50 (0.005)
Coverage (%)	100	100	100
$S_0$	98.96 (0.651)	99.72 (0.816)	98.91 (0.295)
Coverage (%)	100	93	100
Time	1	< 1	72
Data coverage (%)	95.4	98.1	99.8

Table 1: Inference results for the simulated SIR example. For all algorithms, average computing time (minutes), mode of estimates, parameter coverage, and data coverage are computed from 100 simulations. The numbers in the parenthesis indicate the MSE of parameter estimates.

To validate our methods, we repeat the simulation 100 times. Table 1 shows that all methods can recover the true parameters well, though ATVI and ABC show a slight over-coverage. We also examine the performance of our probabilistic projections based on the estimated input parameter densities in terms of MSE and empirical coverage to check the prediction accuracy and uncertainty quantification performance. To be more specific, we compute the mean and the 95% highest posterior density (HPD) intervals for model projections of infected and recovered groups. Then we compute their MSE and empirical coverage by comparing them with the true forward simulation trajectories of the infected and recovered groups. We observe that the

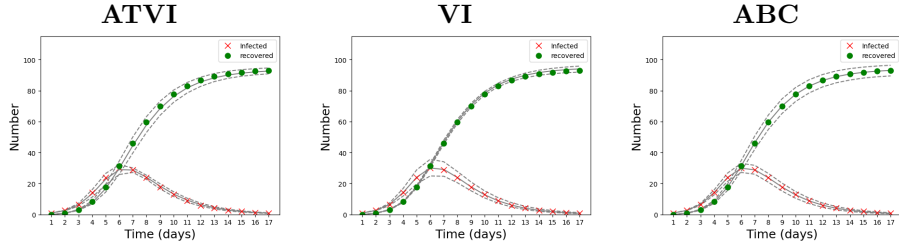


Figure 2: The true number of infected (green dots) and recovered population (red dots) from the basic SIR model. Solid and dashed lines indicate posterior mean and corresponding 95% HPD interval, respectively.

empirical coverage and MSE of parameters are comparable across different methods. However, there is a notable difference in computation time. While the baseline Bayes approach takes about 72 minutes to generate 1,000 accepted samples, both VI approaches take only about a minute.

As an illustrative purpose, we provide a comparison between the assumed true epidemic and the estimated trajectories from a single realization of the repeated simulations (Figure 2). Figure 2 indicates that all algorithms can estimate the true epidemic well; the posterior means and 95% HPD intervals are well-aligned with the simulated epidemics. In summary, VI approaches provide accurate inference results and are more computationally efficient than the ABC algorithm. Note that the performance of ATVI is similar to VI due to the simple structure of the basic SIR model. In the following subsections, we will study challenging examples and show how ATVI has the potential for more significant gains for more complex epidemics.

## 5.2 SEIR Compartment Model Example

Measles is highly contagious and is one of the leading causes of mortality in developing countries. It is an airborne disease, and once infected, most people gain life-long immunity (Barrett, 1987). Though it is relatively preventable with a vaccine, measles is still a common disease in Africa (Lozano et al., 2012). Here, we analyze the 2004 measles outbreak in Malawi data (Minetti et al., 2013). The dataset contains weekly cases and the recorded ratio of the outbreak in three age classes (0.5-5 years, 5-15 years, and 15+ years).

The force of infection for class  $i$  is  $\lambda_i(t) = \beta \sum_j W_{i,j} I_j$ , where  $W$  is a Who Acquire Infection From Whom (WAIFW) matrix (Anderson and May, 1982), which plays a vital role in the age-

structured models. We provide details about the WAIFW matrix in the supplementary material. Following Minter and Retkute (2019), we analyze the measles data using the susceptible-exposed-infected-recovered (SEIR) model as

$$\begin{aligned}\frac{\partial S_i}{\partial t} &= -\frac{\lambda_i S_i}{N} \\ \frac{\partial E_i}{\partial t} &= \frac{\lambda_i S_i}{N} - \frac{1}{7} E_i \\ \frac{\partial I_i}{\partial t} &= \frac{1}{7} E_i - \frac{1}{7} I_i \\ \frac{\partial R_i}{\partial t} &= \frac{1}{7} I_i,\end{aligned}\tag{25}$$

where  $i$  denotes an index for an age class. Compared to the basic SIR model, (25) considers a latent period ( $E_i$ ) during which individuals are infected but not infectious. After the latent period, the individual enters the infectious class with an average latent period of seven days. As in Anderson and May (1985), we assume the average infectious period is also seven days. To model the fraction of each age class, we use the Gamma distribution with shape parameter  $a_{\text{sh}}$  and rate parameter  $a_{\text{rt}}$  as proposed by Shea et al. (2014). Initially exposed population is determined by  $f_E \times N_0$ , where  $N_0$  is a susceptible population size before the outbreak and  $f_E$  is a fraction of the initially exposed.

We use the same prior settings as in Minter and Retkute (2019) (see supplement for details). Note that Minter and Retkute (2019) used two discrepancy terms in the ABC context: (1)  $\delta_1^w$  measures the discrepancies between the simulated infected  $I_w$  and observed infected  $I_w^*$  at the  $w$ th week. (2)  $\delta_2^v$  quantifies the discrepancies between the simulated age population ratio  $p_v$  and the observed age population ration  $p_v^*$  for the  $v$ th age group. Then the proposed samples are accepted when both summary statistics are smaller than the tolerance rates as follows:

$$\sqrt{\sum_w (\delta_1^w)^2} < \epsilon_1, \quad \sqrt{\sum_v (\delta_2^v)^2} < \epsilon_2.$$

As in Minter and Retkute (2019), we set the tolerance rates of the ABC algorithm as  $\epsilon_1 = 10,000$  and  $\epsilon_2 = 0.08$ . For VI approaches, we let  $\delta_1^w \sim N(0, \alpha_1^2)$  and model  $\mathbf{p} = \{p_v\}_{v=1}^3$  with a Dirichlet distribution with concentration parameters defined as  $\alpha_2 \mathbf{p}^*$ . Here  $\mathbf{p}^* = \{p_v^*\}_{v=1}^3$ , where  $p_v^*$  is the observed ratio of outbreak in each class. This model specification sets the expected value of

$\mathbf{p}$  to be  $\mathbf{p}^*$ , while the scalar  $\alpha_2$  controls the variance of the Dirichlet distribution. Here we let  $\alpha_1$  and  $\alpha_2$  take values that generate comparable tolerance levels in Minter and Retkute (2019). Especially, we set  $\alpha_1 = 1400$ , because the ABC algorithm in Minter and Retkute (2019) used a threshold as  $\sqrt{\sum_{w=1}^{53} (\delta_1^w)^2} < \epsilon_1$ . We match the standard deviation of  $\delta_1^w$  and the squared average tolerance  $\sqrt{\epsilon_1^2/53} = 1373.6$  in Minter and Retkute (2019). Similarly, we set  $\alpha_2 = 300$  so that the most mass of the discrepancy is concentrated under the same tolerance level  $\epsilon_2$  in Minter and Retkute (2019) (i.e.,  $P(\sqrt{\sum_v (\delta_2^v)^2} < \epsilon_2 | \alpha_2 = 300) = 0.95$ ).

For both ATVI and VI, we use 20 layers of the flow model with the learning rate of  $6 \times 10^{-4}$ . For ATVI, we set a temperature ladder as  $(t^{(1)}, t^{(2)}) = (10, 1)$ , and each block has ten layers of the flow model. Since reverse KL divergence resulted in reasonable forward results with lower mean squared error, we did not use the last temperature fine-tuning. Following Minter and Retkute (2019), we also implement an ABC sequential Monte Carlo (ABC-SMC) algorithm (Toni et al., 2009) with multivariate normal perturbation kernel; ABC-SMC is an efficient ABC approach where a sequence of distribution is considered with varying tolerance levels. From 500 particles, we generate 5,000 posterior samples from the ABC-SMC algorithm.

	ATVI	VI	ABC-SMC
$\beta \times 10^{-6}$	1.58	1.65	1.31
95% HPD	(1.49, 1.63)	(1.56, 1.76)	(0.96, 2.16)
$N_0 \times 10^3$	207.17	196.24	220.69
95% HPD	(198.57, 213.92)	(186.80, 206.78)	(149.30, 286.33)
$f_E \times 10^{-4}$	2.20	1.86	0.76
95% HPD	(1.46, 3.17)	(1.04, 2.99)	(0.01, 9.17)
$a_{sh}$	0.95	0.99	0.99
95% HPD	(0.89, 1.03)	(0.92, 1.13)	(0.87, 1.05)
$a_{rt} \times 10^{-2}$	9.11	9.80	9.50
95% HPD	(9.00, 9.93)	(9.30, 11.20)	(9.00, 10.30)
Time	5.5	4.8	930
Infected population MSE $\times 10^4$	43.89	47.78	50.73
Age proportion MSE	11.87	18.24	13.58

Table 2: Inference results for the measles dataset. For all methods, mode of estimates, 95% HPD interval, MSE, and computing time (minutes) are reported.

In Table 2, we compare the performance of the three different methods. Although ATVI and VI approximate the same posterior distribution, the ATVI model has a notably lower MSE than the VI model in estimating the age proportion. As described in Section 3.3, VI suffers from the

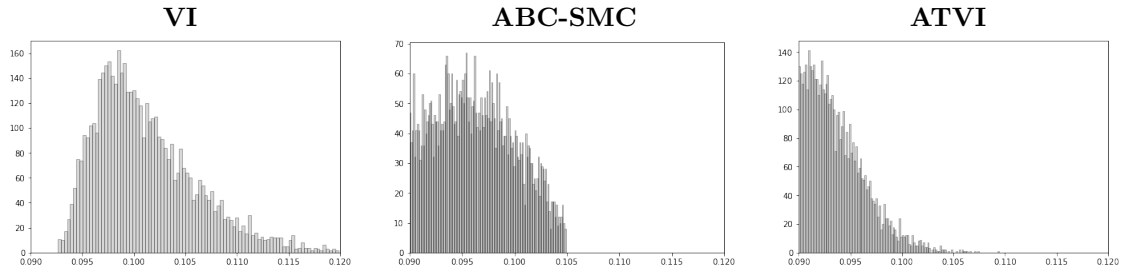


Figure 3: The posterior distributions of the model parameter  $a_{rt}$ .

boundary effect as clearly shown in the posterior distribution of  $a_{rt}$  (Figure 3). ATVI and ABC-SMC, on the other hand, do not have such an issue. The prediction performance of ATVI and ABC-SMC are comparable, but their computing times notably differ. ABC-SMC took almost 15 hours, while ATVI two only took less than 5 minutes. If a tighter tolerance had been used for the ABC-type algorithms, the difference would have been even more significant.

### 5.3 MSIR Compartment Model Example

Rotavirus is the primary reason for diarrheal disease among children and is one of the dominant causes of death (Parashar et al., 2006). However, studying rotavirus dynamics is challenging due to the lack of diagnostic capacity and under-reporting issues; therefore, noisy data are often observed, resulting in difficulties in parameter estimation. Recently, Park et al. (2017) analyzed the rotavirus disease for children in Niger with several variants of disease compartmental models. Here, we examine the MSIR model studied in Park et al. (2017).

The model considers age-structured transmission rates in six groups; 0-1 month, 2-3 months, 4-5 months, 6-11 months, 12-23 months, and 24-59 months. A time-varying transmission rate is

$$\beta_i(t) = \beta_{0i} \left( 1 + w \cos \left( \frac{2\pi t - 52\phi}{52} \right) \right),$$

where  $\beta_{0i}$  is the baseline rate parameter for age class  $i$ ,  $\phi$  is the offset of the seasonal variation, and  $w$  is an amplitude parameter. Then the force of infection, the rate of susceptibles acquiring

rotavirus disease, can be computed as

$$\lambda_i = \sum_{j=1}^6 \beta_j(t) C_{ij} \frac{(I^{(s)} + 0.5I^{(m)})}{N_j},$$

where  $C_{ij}$  is the frequency of contact between the age classes  $i$  and  $j$ , and  $N_j$  is the number of population in the age class  $j$ .  $I^{(s)}$  and  $I^{(m)}$  represent groups infected with severe and mild rotavirus, respectively. From the above specification, the ODE describing rotavirus disease dynamics is

$$\frac{\partial M_i}{\partial t} = \alpha_{i-1} M_{i-1} - \alpha_i M_i + \mu N - \frac{1}{13} M_i \quad (26)$$

$$\frac{\partial S_i}{\partial t} = \alpha_{i-1} S_{i-1} - \alpha_i S_i + \frac{1}{13} M_i - \lambda_i S_i + \frac{1}{52} R_i \quad (27)$$

$$\frac{\partial I_i^{(s)}}{\partial t} = \alpha_{i-1} I_{i-1}^{(s)} - \alpha_i I_i^{(s)} + \frac{6}{25} \lambda_i S_i - I_i^{(s)} \quad (28)$$

$$\frac{\partial I_i^{(m)}}{\partial t} = \alpha_{i-1} I_{i-1}^{(m)} - \alpha_i I_i^{(m)} + \frac{19}{25} \lambda_i S_i - 2I_i^{(m)}. \quad (29)$$

Here, (26) describes the maternal immunity ( $M_i$ ), which is assumed to be 13 weeks. Newborns are added to  $M_i$  with the birth rate  $\mu$ . After a period of maternal immunity, the individual child becomes susceptible ( $S_i$ ) as in (27). Then susceptible individuals can be infected with mild ( $I_i^{(m)}$ ) or severe ( $I_i^{(s)}$ ) rotavirus as described in (28) and (29), respectively. Individuals can leave each state for a mean period of a week (severe) or half a week (mild). If infected children are successfully immunized, they are classified as recovered ( $R_i$ ); even after recovery, individuals may reenter susceptible with a rate of 1/52 (i.e., the mean period of immunity following infection is assumed to be 52 weeks).  $\alpha = \{1/8, 1/8, 1/8, 1/24, 1/48, 1/144\}$  represents the movement rates between age classes. Further model details, including  $C_{ij}$  and  $\mu$  are provided in the supplementary material. Let  $\mathbf{D} = \{D_{i,t}; t \in (1, \dots, 118), i \in (1, \dots, 6)\}$  be the observed data, where  $D_{i,t}$  is the number of reported rotavirus cases in age class  $i$  during week  $t$ . Then  $D_{i,t}$  is modeled via negative binomial distribution with mean  $\eta_i(t) = \frac{6}{25} \rho \lambda_{i,t} S_{i,t}$  and dispersion rate  $\nu$ . Here,  $\eta_i(t)$  is called a disease burden, and  $\rho$  is a reporting rate.

Here, we use synthetic observations that have very similar statistical characteristics to the real observations to avoid data protection issues. We simulated an epidemic from the MSIR model

for given true parameters  $w = 0.43, \phi = 7.35, \rho = 0.027, \nu = 0.9, \beta_{01} = 1.305, \beta_{02} = 3.118, \beta_{03} = 0.032, \beta_{04} = 3.241, \beta_{05} = 0.314, \beta_{06} = 0.094$ ; to consider realistic settings, we used the estimated parameter values in Park et al. (2017). We used uniform priors of model parameters over a plausible range as in Park et al. (2017). Details are provided in the supplementary material.

For both VI approaches, we use 20 layers of the flow model with the learning rate of  $6 \times 10^{-3}$ . For ATVI, we use a temperature ladder as  $(t^{(1)}, t^{(2)}, t^{(3)}) = (12, 3, 1)$ , and each block contains five layers of the flow model. By trying slightly different temperature schedules, we confirmed that the results are not highly sensitive to the choice of temperature schedule. As in Park et al. (2017), we also implement the MCMC algorithm for the MSIR model. We run the adaptive MCMC algorithm (Vihola, 2012) for 50,000 iterations, which can generate an effective sample size between 300 and 1200 (depending on parameters).

	ATVI	VI	MCMC
$w$	0.458 (0.0015)	0.345 (0.0194)	0.467 (0.0021)
Coverage (%)	96	4	94
$\phi$	7.401 (0.0155)	2.281 (26.6225)	7.416 (0.0080)
Coverage (%)	100	4	88
$\rho$	0.026 (0.0000)	0.024 (0.0000)	0.027 (0.0000)
Coverage (%)	90	4	96
$\nu$	0.889 (0.0028)	0.775 (0.0283)	0.902 (0.0019)
Coverage (%)	90	4	100
$\beta_{01}$	1.467 (0.1127)	2.139 (0.2005)	1.785 (0.0788)
Coverage (%)	100	72	80
$\beta_{02}$	3.161 (0.1733)	3.606 (0.1161)	3.258 (0.1797)
Coverage (%)	94	68	98
$\beta_{03}$	0.059 (0.0010)	0.063 (0.0003)	0.397 (0.7842)
Coverage (%)	98	44	94
$\beta_{04}$	3.389 (0.1178)	3.682 (0.0467)	2.997 (0.3056)
Coverage (%)	94	98	92
$\beta_{05}$	0.391 (0.1445)	1.601 (0.6047)	0.335 (0.0073)
Coverage (%)	100	48	98
$\beta_{06}$	0.167 (0.1124)	0.517 (0.1006)	0.101 (0.0005)
Coverage (%)	100	4	96
Computing time (Hours)	1.9	1.1	15.2
Data coverage (%)	96.3	90.6	94.3
Burden estimate coverage (%)	93.5	16.6	93.8

Table 3: Inference results for the simulated rotavirus example. For all algorithms, average computing time (hours), mode of estimates, parameter coverage, and coverages are computed from 50 simulations. The numbers in the parenthesis indicate the MSE of parameter estimates.

We repeat the simulation 50 times to validate our methods, and the results are summarized in

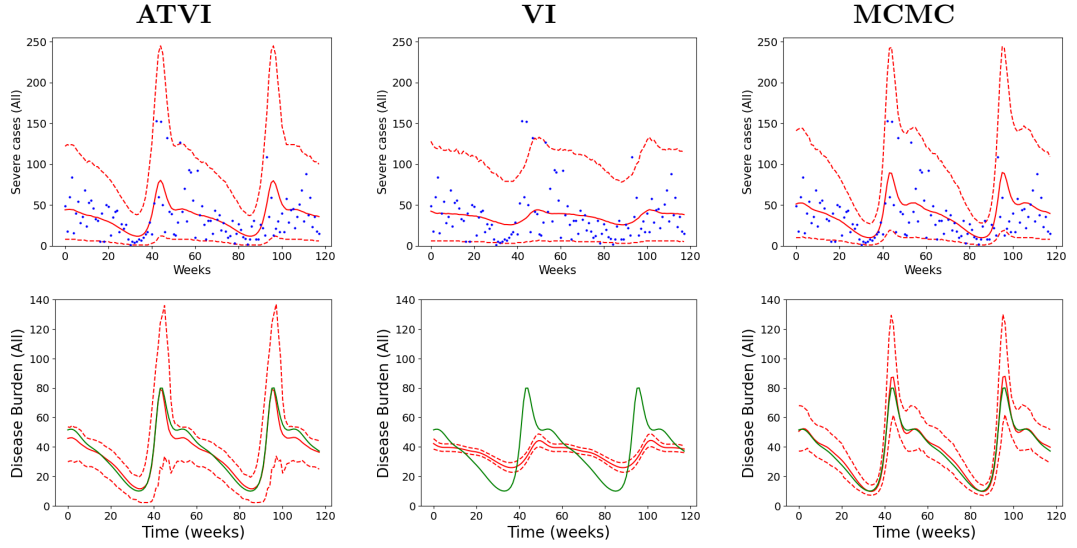


Figure 4: (Top) The observed number of cases (blue dots) and model projection (red lines). (Bottom) The burden estimate (red lines) with the true disease burden (green lines). For all figures, solid and dashed lines indicate posterior mean and corresponding 95% HPD interval, respectively.

Table 3. The parameter estimation results clearly show that ATVI performs comparably to the MCMC in terms of the accuracy of the point estimates as well as the empirical coverage of the interval estimates while enabling much faster computation. On the other hand, VI suffers from a local optima issue due to the complex structure of the forward model; the empirical coverage is unacceptably low for most parameters, and the MSE is much higher than those of ATVI and MCMC for two parameters,  $\phi$  and  $\beta_{05}$ .

As in the previous example, we also evaluate the prediction performance by running the forward model based on the parameter estimates. We first obtain a posterior sample of the total disease burden  $\eta(t) = \sum_{i=1}^6 \eta_i(t)$  based on the MCMC sample for the parameters. Also, we generate simulated observations from the negative binomial distribution with mean  $\eta_i(t)$  and dispersion  $\nu$ . From this, we can obtain the posterior means and the 95% HPD intervals for both the disease burden and the generated observations. Then we compute the empirical coverage of the resulting intervals for their corresponding target quantities, the true disease burden and observations. The results in Table 3 indicate that VI shows notably lower coverage (90.6%) than the nominal rate for the observed data, while ATVI and MCMC algorithms can achieve the

nominal rate. Furthermore, VI shows unacceptably low coverage for the total burden (16.6%), indicating it cannot recover the true disease burden.

We also provide a comparison between the observed cases and model projection from a single realization of the repeated simulations (Figure 4). We observe that the model projections from ATVI and MCMC algorithm recover the disease trend well. In summary, ATVI can provide accurate inference results as the baseline Bayes approach, while it is much faster. Due to the temperature annealing and boundary surjection, ATVI can avoid local optima issues, even for the complicated MSIR model example. The MCMC algorithm will be more expensive if we want to generate a larger number of effective sample sizes than the current settings.

## 6 Discussion

We propose a fast and flexible VI algorithm for compartment model calibration. To construct a variational distribution, we utilize normalizing flows that do not require specific parametric models. Furthermore, we embed surjective transformation and temperature annealing within our framework to alleviate inferential challenges in a naive VI algorithm, boundary and local optima problems when applied to complex compartment models. In the several variants of SIR compartment model examples, ATVI provides comparable inference results as the baseline Bayes approach (e.g., MCMC, ABC), while it is computationally much faster. The ideas and method proposed in this paper can generally be applicable to other calibration tasks such as biochemical models (Hwang et al., 2021) and hydrological models (Gochis et al., 2018).

There can be several improvements for ATVI from an algorithmic perspective. We observed that sequentially annealed posteriors were not sensitive depending on the temperature ladder once we set the first temperature to be high enough. However, developing an adaptive temperature schedule in ATVI would result in a more automatic algorithm. Furthermore, selecting a specific divergence for variational inference remains an open question. Since there are many divergences with various trade-offs (Regli and Silva, 2018), selecting a specific divergence for variational inference remains an open question. The Real NVP model was flexible enough to capture the posterior density in our application problems. However, a more flexible and theoretically justified model may be necessary for other situations. A closer examination of adopting such an approach

as autoregressive models (Papamakarios et al., 2021, Huang et al., 2018) would be an interesting future research avenue.

## Acknowledgement

Jaewoo Park and Dongkyu Cho were supported by the National Research Foundation of Korea (NRF-2020R1C1C1A0100386813). The authors are grateful to anonymous reviewers for their careful reading and valuable comments.

## References

- Anderson, R. and R. May (1982). Control of communicable diseases by age-specific immunisation schedules. *The Lancet* 319(8264), 160.
- Anderson, R. and R. May (1985). Age-related changes in the rate of disease transmission: implications for the design of vaccination programmes. *Epidemiology & Infection* 94(3), 365–436.
- Arenz, O., M. Zhong, and G. Neumann (2020). Trust-region variational inference with gaussian mixture models. *J. Mach. Learn. Res.* 21, 163–1.
- Barrett, T. (1987). The molecular biology of the morbillivirus (measles) group. In *Biochemical Society Symposium*, Volume 53, pp. 25–37.
- Bayarri, M., J. Berger, J. Cafeo, G. Garcia-Donato, F. Liu, J. Palomo, R. Parthasarathy, R. Paulo, J. Sacks, and D. Walsh (2007). Computer model validation with functional output. *the Annals of Statistics* 35(5), 1874–1906.
- Beaumont, M. A., W. Zhang, and D. J. Balding (2002). Approximate Bayesian computation in population genetics. *Genetics* 162(4), 2025–2035.
- Berg, R. v. d., L. Hasenclever, J. M. Tomczak, and M. Welling (2018). Sylvester normalizing flows for variational inference. *arXiv preprint arXiv:1803.05649*.

- Bhat, K., M. Haran, R. Olson, and K. Keller (2012). Inferring likelihoods and climate system characteristics from climate models and multiple tracers. *Environmetrics* 23(4), 345–362.
- Bhatnagar, S., W. Chang, and S. K. J. Wang (2022). Computer model calibration with time series data using deep learning and quantile regression. *SIAM/ASA Journal on Uncertainty Quantification* 10(1), 1–26.
- Bjørnstad, O. N., B. F. Finkenstädt, and B. T. Grenfell (2002). Dynamics of measles epidemics: estimating scaling of transmission rates using a time series sir model. *Ecological monographs* 72(2), 169–184.
- Blei, D. M., A. Kucukelbir, and J. D. McAuliffe (2017). Variational inference: A review for statisticians. *Journal of the American statistical Association* 112(518), 859–877.
- Bond-Taylor, S., A. Leach, Y. Long, and C. G. Willcocks (2021). Deep generative modelling: A comparative review of vaes, gans, normalizing flows, energy-based and autoregressive models. *arXiv preprint arXiv:2103.04922*.
- Bornschein, J. and Y. Bengio (2014). Reweighted wake-sleep. *arXiv preprint arXiv:1406.2751*.
- Chang, W., M. Haran, P. Applegate, and D. Pollard (2016). Calibrating an ice sheet model using high-dimensional binary spatial data. *Journal of American Statistical Association* 111(513), 57–72.
- Chang, W., M. Haran, R. Olson, and K. Keller (2014). Fast dimension-reduced climate model calibration and the effect of data aggregation. *AOAS* 8(2), 649–673.
- Dietz, K. (1967). Epidemics and rumours: A survey. *Journal of the Royal Statistical Society. Series A (General)*, 505–528.
- Dinh, L., J. Sohl-Dickstein, and S. Bengio (2016). Density estimation using real nvp. *arXiv preprint arXiv:1605.08803*.
- Gochis, D., M. Barlage, A. Dugger, K. FitzGerald, L. Karsten, M. McAllister, J. McCreight, J. Mills, A. RafieeiNasab, L. Read, et al. (2018). The WRF-Hydro modeling system technical description,(version 5.0). *NCAR Technical Note* 107.

- Higdon, D., J. Gattiker, B. Williams, and M. Rightley (2008). Computer model calibration using high-dimensional output. *Journal of American Statistical Association* 103(482), 570–583.
- Huang, C.-W., D. Kruseger, A. Lacoste, and A. Courville (2018). Neural autoregressive flows. In *International Conference on Machine Learning*, pp. 2078–2087. PMLR.
- Hwang, Y., H. J. Kim, W. Chang, C. Hong, and S. N. MacEachern (2021). A bayesian solution to inverse problem for circadian cycles. *arXiv preprint arXiv:2110.10604*.
- Jerfel, G., S. Wang, C. Wong-Fannjiang, K. A. Heller, Y. Ma, and M. I. Jordan (2021). Variational refinement for importance sampling using the forward kullback-leibler divergence. In *Uncertainty in Artificial Intelligence*, pp. 1819–1829. PMLR.
- Katahira, K., K. Watanabe, and M. Okada (2008). Deterministic annealing variant of variational bayes method. In *Journal of Physics: Conference Series*, Volume 95, pp. 012015. IOP Publishing.
- Keeling, M. J. and P. Rohani (2011). *Modeling infectious diseases in humans and animals*. Princeton university press.
- Kennedy, M. C. and A. O'Hagan (2001). Bayesian calibration of computer models. *Journal of the Royal Statistical Society: Series B (Statistical Methodology)* 63(3), 425–464.
- Kermack, W. O. and A. G. McKendrick (1927). A contribution to the mathematical theory of epidemics. *Proceedings of the royal society of london. Series A, Containing papers of a mathematical and physical character* 115(772), 700–721.
- Kingma, D. P. and P. Dhariwal (2018). Glow: Generative flow with invertible 1x1 convolutions. *Advances in neural information processing systems* 31.
- Kingma, D. P., T. Salimans, R. Jozefowicz, X. Chen, I. Sutskever, and M. Welling (2016). Improved variational inference with inverse autoregressive flow. *Advances in neural information processing systems* 29.
- Kingma, D. P. and M. Welling (2013). Auto-encoding variational bayes. *arXiv preprint arXiv:1312.6114*.

- Kobyzev, I., S. J. Prince, and M. A. Brubaker (2020). Normalizing flows: An introduction and review of current methods. *IEEE transactions on pattern analysis and machine intelligence* 43(11), 3964–3979.
- Kucukelbir, A., D. Tran, R. Ranganath, A. Gelman, and D. M. Blei (2017). Automatic differentiation variational inference. *Journal of machine learning research*.
- Li, Y. and R. E. Turner (2016). Rényi divergence variational inference. *Advances in neural information processing systems* 29.
- Lozano, R., M. Naghavi, K. Foreman, S. Lim, K. Shibuya, V. Aboyans, J. Abraham, T. Adair, R. Aggarwal, S. Y. Ahn, et al. (2012). Global and regional mortality from 235 causes of death for 20 age groups in 1990 and 2010: a systematic analysis for the global burden of disease study 2010. *The lancet* 380(9859), 2095–2128.
- Mandt, S., J. McInerney, F. Abrol, R. Ranganath, and D. Blei (2016). Variational tempering. In *Artificial intelligence and statistics*, pp. 704–712. PMLR.
- Marin, J.-M., P. Pudlo, C. P. Robert, and R. J. Ryder (2012). Approximate Bayesian computational methods. *Statistics and Computing* 22(6), 1167–1180.
- Minetti, A., M. Kagoli, A. Katsulukuta, H. Huerga, A. Featherstone, H. Chiotcha, D. Noel, C. Bopp, L. Sury, R. Fricke, et al. (2013). Lessons and challenges for measles control from unexpected large outbreak, malawi. *Emerging infectious diseases* 19(2), 202.
- Minter, A. and R. Retkute (2019). Approximate bayesian computation for infectious disease modelling. *Epidemics* 29, 100368.
- Neal, R. M. (2001). Annealed importance sampling. *Statistics and computing* 11(2), 125–139.
- Nielsen, D., P. Jaini, E. Hoogeboom, O. Winther, and M. Welling (2020). Survae flows: Surjections to bridge the gap between vaes and flows. *Advances in Neural Information Processing Systems* 33, 12685–12696.
- Papamakarios, G., E. Nalisnick, D. J. Rezende, S. Mohamed, and B. Lakshminarayanan (2021). Normalizing flows for probabilistic modeling and inference. *Journal of Machine Learning Research* 22(57), 1–64.

- Parashar, U. D., C. J. Gibson, J. S. Bresee, and R. I. Glass (2006). Rotavirus and severe childhood diarrhea. *Emerging infectious diseases* 12(2), 304.
- Park, J., J. Goldstein, M. Haran, and M. Ferrari (2017). An ensemble approach to predicting the impact of vaccination on rotavirus disease in niger. *Vaccine* 35(43), 5835–5841.
- Pitzer, V. E., K. E. Atkins, B. F. de Blasio, T. Van Effelterre, C. J. Atchison, J. P. Harris, E. Shim, A. P. Galvani, W. J. Edmunds, C. Viboud, et al. (2012). Direct and indirect effects of rotavirus vaccination: comparing predictions from transmission dynamic models.
- Plumlee, M. (2017). Bayesian calibration of inexact computer models. *Journal of the American Statistical Association* 112(519), 1274–1285.
- Plumlee, M. (2019). Computer model calibration with confidence and consistency. *Journal of the Royal Statistical Society: Series B (Statistical Methodology)* 81(3), 519–545.
- Ranganath, R., D. Tran, J. Altosaar, and D. Blei (2016). Operator variational inference. *Advances in Neural Information Processing Systems* 29.
- Regli, J.-B. and R. Silva (2018). Alpha-beta divergence for variational inference. *arXiv preprint arXiv:1805.01045*.
- Rezende, D. and S. Mohamed (2015). Variational inference with normalizing flows. In *International conference on machine learning*, pp. 1530–1538. PMLR.
- Shea, K., M. J. Tildesley, M. C. Runge, C. J. Fonnesbeck, and M. J. Ferrari (2014). Adaptive management and the value of information: learning via intervention in epidemiology. *PLoS biology* 12(10), e1001970.
- Toni, T., D. Welch, N. Strelkowa, A. Ipsen, and M. P. Stumpf (2009). Approximate Bayesian computation scheme for parameter inference and model selection in dynamical systems. *Journal of the Royal Society Interface* 6(31), 187–202.
- Tuo, R. and C. J. Wu (2015). Efficient calibration for imperfect computer models. *the Annals of Statistics* 43(6), 2331–2352.

- Turner, R. E. and M. Sahani (2011). Two problems with variational expectation maximisation for time-series models. In D. Barber, T. Cemgil, and S. Chiappa (Eds.), *Bayesian Time series models*, Chapter 5, pp. 109–130. Cambridge University Press.
- Vehtari, A., D. Simpson, A. Gelman, Y. Yao, and J. Gabry (2015). Pareto smoothed importance sampling. *arXiv preprint arXiv:1507.02646*.
- Vihola, M. (2012). Robust adaptive metropolis algorithm with coerced acceptance rate. *Statistics and Computing* 22(5), 997–1008.
- Zhang, C., J. Bütepage, H. Kjellström, and S. Mandt (2018). Advances in variational inference. *IEEE transactions on pattern analysis and machine intelligence* 41(8), 2008–2026.

# Supplementary Material for Fast Compartment Model Calibration using Annealed and Transformed Variational Inference

Dongkyu Cho, Won Chang, and Jaewoo Park

November 22, 2022

## 1 Prior Settings

Parameter	Definition	Prior
$\beta$	Transmission rate per day	Uniform (0, 3)
$\gamma$	Recovery rate per day	Uniform (0, 1)
$S_0$	Initial number of susceptibles	Uniform (80, 120)

Table 1: Prior distributions for the SIR model parameters.

Parameter	Definition	Prior
$\beta$	Transmission rate per day	Uniform (0, $5 \times 10^{-6}$ )
$N_0$	Susceptible population size before outbreak	Uniform ( $140 \times 10^3$ , $300 \times 10^3$ )
$f_E$	Fraction of initially exposed	Uniform (0, $1 \times 10^{-3}$ )
$a_{sh}$	Shape parameter for age distribution	Uniform (0.8, 1.4)
$a_{rt}$	Rate parameter for age distribution	Uniform (0.09, 0.4)

Table 2: Prior distributions of SEIR model parameters

Parameter	Definition	Prior
$w$	Amplitude of transmission rate	Uniform (0, 1)
$\phi$	Offset of the seasonal variation	Uniform (2, 8.28)
$\nu$	Dispersion rate	Uniform (0.5, 1)
$\rho$	Reporting rate	Uniform (0, 1)
$\beta_{0i}$	Base rate parameter for age class $i$ , $i \in \{1, 2, \dots, 6\}$	Uniform (0, 4)

Table 3: Prior distributions for the MSIR model parameters

## 2 Model Details

### 2.1 SEIR Model

Anderson and May (1982) introduced the Who Acquire Infection From Whom (WAIFW) matrix to construct age-structured compartment models. As in Shea et al. (2014), we use the WAIF matrix as

$$W = \begin{bmatrix} 1 & \frac{11}{12} & \frac{5}{6} & \frac{3}{4} & \frac{2}{3} & \dots & \frac{2}{3} \\ \frac{11}{12} & 1 & \frac{11}{12} & \frac{5}{6} & \frac{3}{4} & \dots & \frac{2}{3} \\ \frac{5}{6} & \frac{11}{12} & 1 & \frac{11}{12} & \frac{5}{6} & \dots & \frac{2}{3} \\ \frac{3}{4} & \frac{5}{6} & \frac{11}{12} & 1 & \frac{11}{12} & \dots & \frac{2}{3} \\ \frac{2}{3} & \frac{3}{4} & \frac{5}{6} & \frac{11}{12} & 1 & \dots & \frac{2}{3} \\ \dots & \dots & \dots & \dots & \dots & \dots & \dots \\ \frac{2}{3} & \frac{2}{3} & \frac{2}{3} & \frac{2}{3} & \frac{2}{3} & \dots & 1 \end{bmatrix}$$

In age-structured models, age groups play a vital role. In this example, we have 22 age classes: 6-12 months, 1-2 years, 2-3 years, ..., 19-20 years, and 20+ years.

### 2.2 MSIR Model

Park et al. (2017) assumed the birth rate  $\mu(t)$  changes over time. Park et al. (2017) considered the mean weekly birth rate as  $\bar{\mu} = 1/(5 \times 52)$  with variation in monthly birth rate (Table 4). Seasonal variation in the birth rate in Niger is estimated from Demographic and Health Surveys (Dorélien, 2013).

Jan	Feb	Mar	Apr	May	Jun	Jul	Aug	Sep	Oct	Nov	Dec
-0.17	0.01	0.03	0.25	0.12	0.03	-0.01	0.09	0.01	0.13	-0.31	-0.17

Table 4: Seasonable variation in the birth rate.

As in Park et al. (2017), we use a contact matrix

$$C = \begin{bmatrix} 1 & 1 & 1 & 1 & 1 & 1 \\ 1 & 1 & 1 & 1 & 1 & 1 \\ 1 & 1 & 1 & 1 & 1 & 1 \\ 3 & 3 & 3 & 1 & 1 & 1 \\ 6 & 6 & 6 & 2 & 1 & 1 \\ 18 & 18 & 18 & 6 & 3 & 1 \end{bmatrix}$$

Here,  $C_{ij}$  denotes the frequency of contact between age class  $i$  and  $j$ , satisfying  $f_i C_{ij} = f_j C_{ji}$ , where  $f_i$  is the fraction of the age group  $i$  of the population. The model using such a contact matrix assumes that the contact between age groups is homogeneous. Furthermore, Park et al. (2017) only considered transmission between children and assumed the population of children is closed.

### 2.3 Additional results

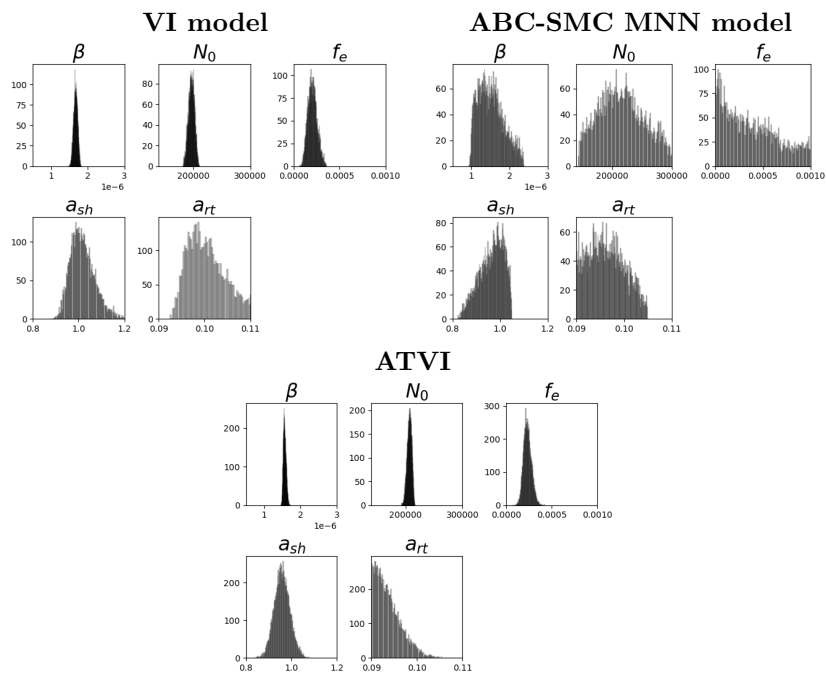


Figure 1: The posterior distributions of the model parameters.

### 3 Proof of the Main Results

#### 3.1 Proposition 1

**Proof** For any given density, we can consider the surjective transformation approximation as

$$\mathbb{E}_{v_{\theta}(\theta|\xi)} [\log p_{\theta}(\theta)] = \log p_{\xi}(\xi) - \mathcal{V}(\theta, \xi) - \mathcal{E},$$

which follows from the results in Nielsen et al. (2020). Then the approximation error  $\mathcal{E}$  can be written as

$$\mathcal{E} = \log p_{\xi}(\xi) - \mathbb{E}_{v_{\theta}(\theta|\xi)} [\log p_{\theta}(\theta)] - \mathcal{V}(\theta, \xi) \quad (\text{S1})$$

$$= \mathbb{E}_{v_{\theta}(\theta|\xi)} \left[ \log \frac{v_{\theta}(\theta|\xi)}{w_{\theta}(\theta|\xi)} \right], \quad (\text{S2})$$

where  $w_{\theta}(\theta|\xi) = \frac{p(\theta)}{p(\xi)} w_{\xi}(\xi|\theta)$  using Bayes rule. By the definition of  $w_{\xi}(\xi|\theta)$  in Section 4.1 (16),  $\mathcal{B}(\xi) = \theta$  holds  $\forall \xi$  following the distribution with the density  $w_{\xi}(\xi|\theta)$ . This implies  $\forall \xi \in \mathcal{B}^{-1}(\Theta)$ , there is an unique  $\theta \in \Theta$  that makes  $w_{\xi}(\xi|\theta) > 0$ , resulting in  $w_{\theta}(\theta|\xi) = \delta(\theta - \mathcal{B}(\xi))$ . Likewise, by the definition of  $v_{\theta}(\theta|\xi)$  in Section 4.1 (15),  $v_{\theta}(\theta|\xi) = \delta(\theta - \mathcal{B}(\xi))$  holds  $\forall \xi \in \mathcal{B}^{-1}(\Theta)$ . We now have  $w_{\theta}(\theta|\xi) = v_{\theta}(\theta|\xi)$ , and the approximation error  $\mathcal{E}$  becomes zero.

Now, consider  $\mathbb{E}_{v_{\theta}(\theta|\xi)} [\log p_{\theta}(\theta)]$ , the second term (S1). As  $v_{\theta}(\theta|\xi) = \delta(\theta - \mathcal{B}(\xi))$ , the term becomes  $\log p_{\theta}(\theta)$ . Hence, we have the following equation:

$$\log p_{\theta}(\theta) = \log p_{\xi}(\xi) - \mathcal{V}(\theta, \xi).$$

□

### 3.2 Proposition 2

**Proof** Consider the logarithm of the target density  $\log p_{\xi}(\xi|\mathbf{D}) = \log p_{\theta}(\theta|\mathbf{D}) + \mathcal{V}(\theta, \xi)$ , where

$$\begin{aligned}\mathcal{V}(\theta, \xi) &= \sum_{i=1}^d \log w_{s_i}(s_i|\theta_i) = \sum_{i=1}^d \delta(s_i = g_2(\xi_i)) \log w_{s_i}(s_i|\theta_i) \\ &= \sum_{i=1}^d [\delta(0 = g_2(\xi_i)) \log(1 - u_i(\theta_i)) + \delta(1 = g_2(\xi_i)) \log(u_i(\theta_i))].\end{aligned}$$

The second equality holds because we set  $g_2(\xi_i) = s_i$ . As both  $p_{\theta}(\theta|\mathbf{D})$  and  $u_i(\theta_i)$  are continuous functions, we only need to show that  $\mathcal{V}(\theta, \xi)$  is continuous at the parameter boundary (i.e.,  $\xi_i \rightarrow a_i$  for some  $i$ ). Due to the Condition 2,  $\forall i$ ,  $u_i(a_i) = 1 - u_i(a_i) = 0.5$  and thus  $p_{\xi}(\xi|\mathbf{D})$  is continuous.

Consider a point  $\mathbf{k} \in \prod_{i=1}^d (-\infty, a_i - r) \cap \mathcal{B}^{-1}(\Theta)$ . Then we have the following result.

$$\mathcal{V}(\theta = 2\mathbf{a} - \mathbf{k}, \xi = \mathbf{k}) = \sum_{i=1}^d [\delta(0 = g_2(k_i)) \log(1 - u_i(2a_i - k_i))] = \sum_{i=1}^d [\log(1 - u_i(2a_i - k_i))]$$

The equalities hold due to the fact that  $\mathcal{B}(\mathbf{k}) = 2\mathbf{a} - \mathbf{k}$  and  $\forall i$ ,  $g_2(k_i) = 0$ . Then we have

$$\begin{aligned}p_{\xi}(\mathbf{k}|\mathbf{D}) &= p_{\xi}(\mathbf{k}|\mathbf{D}) \prod_{i=1}^d (1 - u_i(2a_i - k_i)) \\ &\leq M \prod_{i=1}^d \sqrt[d]{\epsilon/M} = \epsilon\end{aligned}$$

from Condition 3. Hence,  $p_{\xi}(\mathbf{k}|\mathbf{D}) \leq \epsilon$ . The Condition 4 is equivalent to

$$\begin{aligned}\frac{\partial u_i(c_i)}{\partial c_i} (1 - u_i(c_i))^{-1} &\geq \frac{\partial p_{\theta}(\mathbf{c}|\mathbf{D})}{\partial c_i} (p_{\theta}(\mathbf{c}|\mathbf{D}))^{-1} \\ \Leftrightarrow \frac{\partial u_i(c_i)}{\partial c_i} p_{\theta}(\mathbf{c}|\mathbf{D}) - (1 - u_i(c_i)) \frac{\partial p_{\theta}(\mathbf{c}|\mathbf{D})}{\partial c_i} &\geq 0 \\ \Leftrightarrow \prod_{j \neq i} (1 - u_j(c_j)) \frac{\partial u_i(c_i)}{\partial c_i} p_{\theta}(\mathbf{c}|\mathbf{D}) - \prod_j (1 - u_j(c_j)) \frac{\partial p_{\theta}(\mathbf{c}|\mathbf{D})}{\partial c_i} &\geq 0 \\ \Leftrightarrow \frac{\partial \left( \prod_j (1 - u_j(c_j)) p_{\theta}(\mathbf{c}|\mathbf{D}) \right)}{\partial(-c_i)} &\geq 0 \\ \Leftrightarrow \frac{\partial p_{\xi}(2\mathbf{a} - \mathbf{c}|\mathbf{D})}{\partial(-c_i)} &\geq 0,\end{aligned}$$

where the last equivalence comes from the fact that  $\mathcal{B}(2\mathbf{a} - \mathbf{c}) = \mathbf{c}$  and  $\forall i, g_2(2a_i - c_i) = 0$ . Therefore,  $p_{\xi}(\xi|\mathbf{D})$  is a monotone increasing function within  $\prod_{i=1}^d [a_i - r, a_i] = \mathcal{Q}_{r-}(\mathbf{a})$ . For the transformed approximated distribution, we have  $\log q_{\theta}(\theta; \phi) = \log q_{\xi}(\xi; \phi) - \mathcal{V}(\theta, \xi)$ . Since the Proposition 1 ensures  $u_i(\theta_i)$  and  $1 - u_i(\theta_i)$  are both in class of  $C^{\infty}$ ,  $\mathcal{V}(\theta, \xi) \in C^{\infty}(\mathcal{Q}_{r+}(\mathbf{a}))$ . Thus,  $q_{\theta}(\theta; \phi) \in C^m(\mathcal{Q}_{r+}(\mathbf{a}))$   $\square$

### 3.3 Remark

**Proof** Obviously,  $\varsigma_i(x; a_i, B)$  satisfies the first and second conditions. Further, note that  $\varsigma_i(B; a_i, x)$  is an strictly increasing function with respect to  $B$ , such that  $\varsigma_i(B; a_i, x) : (-\infty, \infty) \rightarrow (0, 1)$  for  $x \in [a_i, \infty)$ . For some small  $r \in (0, \frac{b_i - a_i}{2})$ , we can find a  $B$  that is large enough to satisfy the third condition. Now, note a derivative of the logistic function can be written as follows:

$$\frac{\partial \varsigma_i(x; A, 1)}{\partial x} = \varsigma_i(x; A, 1) (1 - \varsigma_i(x; A, 1)).$$

Therefore,  $\frac{\partial \varsigma_i(x; A, B)}{\partial x} = B \varsigma_i(x; A, B) (1 - \varsigma_i(x; A, B))$ . The left term of Condition 4 in Proposition 2 now becomes identical to Section 4.2 (18) because

$$\begin{aligned} \frac{\partial \varsigma_i(c_i; a_i, B)}{\partial c_i} (1 - \varsigma_i(c_i; a_i, B))^{-1} &= \frac{B \varsigma_i(c_i; a_i, B) (1 - \varsigma_i(c_i; a_i, B))}{1 - \varsigma_i(c_i; a_i, B)} \\ &= B \varsigma_i(c_i; a_i, B) \end{aligned}$$

$\square$

## References

- Anderson, R. and R. May (1982). Control of communicable diseases by age-specific immunisation schedules. *The Lancet* 319(8264), 160.
- Dorélien, A. M. (2013). A time to be born: birth seasonality in sub-Saharan Africa. *University of Michigan Population Studies Center Research Report Series Report 13*(785), 1–61.
- Nielsen, D., P. Jaini, E. Hoogeboom, O. Winther, and M. Welling (2020). Survae flows: Surjec-

tions to bridge the gap between vaes and flows. *Advances in Neural Information Processing Systems* 33, 12685–12696.

Park, J., J. Goldstein, M. Haran, and M. Ferrari (2017). An ensemble approach to predicting the impact of vaccination on rotavirus disease in niger. *Vaccine* 35(43), 5835–5841.

Shea, K., M. J. Tildesley, M. C. Runge, C. J. Fonnesbeck, and M. J. Ferrari (2014). Adaptive management and the value of information: learning via intervention in epidemiology. *PLoS biology* 12(10), e1001970.